Exhuming the Canadian Shield: preliminary interpretations from low-temperature thermochronology and significance for the sedimentary succession of the Hudson Bay Basin

EarthArXiv preprint, compiled May 21, 2021

Kalin T. McDannell [1,2*], **Nicolas Pinet**[3], **and Dale R. Issler** [1]

[1]Natural Resources Canada, Geological Survey of Canada, 3303-33rd Street N.W., Calgary, Alberta T2L 2A7
[2]Present address: Department of Earth Sciences, Dartmouth College, 6105 Fairchild Hall, Hanover, NH 03775 USA
[3]Natural Resources Canada, Geological Survey of Canada, 490 rue de la Couronne, Québec, Quebec G1K 9A9

Abstract

The geological history of the Canadian Shield is difficult to constrain because the sedimentary record is missing in those areas where Precambrian basement is exposed at the surface. This study presents preliminary results and interpretations of new apatite fission-track (AFT) analyses to elucidate the low-temperature (< 120 °C) history across Canada. The AFT modelling of samples from Southampton Island, in Nunavut, indicate that maximum temperatures varied between 62–93 °C during the Phanerozoic. Maximum burial occurred in the Devonian, but a second phase of Mesozoic burial is proposed, especially in the case for the sample recovered closest to the northern island-bounding normal faults. The AFT modelling of a sample from northern Ontario indicates that a maximum burial temperature of approximately 75 °C was reached during the Late Devonian. Overall, these results demonstrate that the Hudson Bay sedimentary succession is the remnant of a more extensive and thicker sedimentary cover than is preserved. This study also provides the opportunity to discuss innovative methodology and modelling approaches for low-temperature thermochronology.

This manuscript has been submitted for publication in *Geological Survey of Canada Bulletin 609: Sedimentary basins of the Canadian north — contributions to a 1000 Ma geological journey and insight on resource potential, Chapter 10*. Please note that, despite having undergone peer-review, this manuscript has not been fully accepted in print and is undergoing multi-year editorial production before final publication. Future versions may contain slightly different content—please contact the authors with any questions.

Recommended *in press* citation: *McDannell, K.T., Pinet, N., and Issler, D.R., in press, Exhuming the Canadian Shield: preliminary interpretations from low-temperature thermochronology and significance for the sedimentary succession of the Hudson Bay Basin; in Sedimentary basins of the Canadian north — contributions to a 1000 Ma geological journey and insight on resource potential; (ed.) D. Lavoie and K. Dewing; Geological Survey of Canada, Bulletin 609, p. xx–xx. https://doi.org/10.4095/xxxxxx*

1 INTRODUCTION

The assembly of lithospheric blocks that formed the core of the North American continent was completed by the end of the Neoproterozoic and most of the geological and geophysical characteristics of the Canadian Shield were acquired before the Phanerozoic [1, 2, 3]. The typical view of cratons is that they stabilized in the Archean and behaved as passive lithospheric blocks, undergoing steady erosion during times of low sea level and sedimentary deposition during periods of high sea level. The lack of evidence for significant tectonic activity since the Cambrian and the fragmented nature of the sedimentary record have been used to imply that the shield was stable during the last 500 Ma, registering only minor sedimentary (or ice-loading) events. A 'uniform' exhumation model, in which the Canadian Shield reacted as a single entity and experienced a slow, protracted exhumation at more or less uniform rates across thousands of kilometres, has been the dominant paradigm among Earth scientists [e.g., 4]. This assessment is broadly consistent with some studies that suggest distinctive examples of long-term continental exhumation rates that are extremely low (< 2.5 m/Myr) and have been for many hundreds of millions to billions of years [5, 6]. However, in recent years it has become more apparent that cratons are more dynamic, having been acted upon by plate tectonics, mantle flow, and surficial processes at time scales of 10^8 to 10^9 years [e.g., 7, 8, 9]. There are examples, such as the South African and North China cratons, that are currently in a state of (topographic or lithospheric) disequilibrium due to mantle upwelling [10, 11, 12], which indicates that cratons undergo periodic disruption over shorter time scales of 10^5 to 10^7 years. Exhumation may appear to be slow over billions of years, based on thermochronological studies, but cratonic interiors likely experienced punctuated episodes of more rapid erosion or burial that are either, 1) difficult to capture due to low signal/noise, or 2) simply represent a lack of both spatial and temporal coverage in existing thermochronology studies to identify and quantify these events during an otherwise monotonous long-term history.

This Geological Survey of Canada (GSC) project was initiated under the Geo-mapping for Energy and Minerals (GEM-2) program to investigate the exhumation and burial history of the Canadian craton at the continental scale. The basic idea underpinning the project was that the quantification of the magnitude and timing of past heating (a proxy for sedimentary burial) and cooling (a proxy for erosional exhumation) would provide thickness estimates of the now-eroded Phanerozoic cover rocks and be instrumental in assessing the petroleum potential of intracratonic and Arctic basins. Constraining the Paleozoic to present exhumation history at the continental scale could point to unexpected linkages between basins with known and unknown petroleum prospectivity. Moreover, spatiotemporal patterns of temperature changes may be potentially linked with geodynamic events that shaped North America during the Phanerozoic, providing a window on geological processes that act at the continental scale. The new data set also provides an opportunity to discuss cutting-edge analytical and interpretive aspects of low-temperature thermochronology methods and modelling strategies for slowly cooled terranes. Additional overviews

*correspondence: kalin.t.mcdannell@dartmouth.edu

and examples of low-temperature thermochronology applied to cratons and slowly cooled regions can be found in Green and Duddy [13], Flowers [14], McDannell [15], McDannell et al. [16], Kohn and Gleadow [17], and McDannell and Flowers [18].

Apatite fission-track (AFT) and apatite (U-Th-Sm)/He (AHe) dating provide independent sets of information sensitive to the thermal histories of rocks typically between ~60 ° and 110 °C and ~40 ° and 80 °C, respectively. These methods are sensitive to cooling (exhumation) events that are unlikely to be captured by basin models solely based on conventional thermal-maturity indicators (i.e., vitrinite reflectance (%Ro), T_{max}, fluid inclusions, or clumped isotopes) because modelling of AFT and AHe data documents both temporal and paleotemperature evolution.

2 APATITE FISSION-TRACK (AFT) THERMOCHRONOLOGY

2.1 AFT method

The bulk of the craton thermochronology was carried out using apatite fission-track analysis, therefore (U-Th)/He dating will not be discussed in detail. A comprehensive overview of fission-track dating and the theoretical background is given in Donelick et al. [19] and Tagami and O'Sullivan [20]. In this paper, a few of the more important aspects relating to fission-track theory and application are discussed.

Uranium- and thorium-bearing minerals such as apatite ($Ca_5(PO_4)_3$[F, Cl, OH]) primarily undergo continuous, spontaneous ^{238}U α-decay, with the majority of radiation damage produced by alpha recoil in the apatite lattice, whereas fission is a minor contributor to the total accrued damage [e.g., 19]. During fission events, positive ions created by the transmission of highly charged fission fragments repel one another and form a cylindrical region of crystal damage, referred to as a 'fission track' [FT; 21, 22, 23, 24]. Based on these physical principles, AFT thermochronology is a radiometric dating technique that follows the classic isotopic parent-daughter decay scheme, where ^{238}U is the parent and the daughter product is not an isotope but is the damage trail produced by fission. Ages are calculated by relating the amount of crystalline track damage per area (FT density, or daughter product) to the amount of ^{238}U (parent isotope). The fission track 'apparent age' is proportional to the amount of time that has passed since fission tracks appreciably accumulated within the crystal lattice. This process is temperature dependent and typically tracks do not accumulate at temperatures higher than 125 °C in common fluorapatite [25]. Fission-track ages are useful in determining timing of cooling through approximately 100 °C for fluorapatite, whereas measuring confined track-length distributions yields information regarding thermal-history style [26, 27].

Fission-track annealing within apatite is mainly influenced by magnitude and duration of heating, which results in the reduction of track length(s) and track density in the apatite volume [25, 28, 29, 30]. Apatite chemical composition also affects FT annealing kinetics (i.e., lattice-site substitutions). Chlorine content has been identified as a primary control on fission-track retentivity [28]. Subsequent experiments found that other hydroxyl and cation substituents such as OH^-, Fe^2+, Na^+, Si, and REE are also important in regulating FT retention [31, 32, 33, 34, 35, 36, 37].

Apatite fission-track ages seldom date the timing of a geological event, but instead are a reflection of the integrated thermal history experienced by rocks in the upper few kilometres of the crust (~3–4 km, or more under low thermal gradients). This may be a result of any of the following processes: broad-scale tectonism or tilting, orogenic uplift, fluvial or glacial erosional denudation, burial heating, fault movement, and changes in heat or fluid flow. A recent overview and examples of applied studies can be found in Malusà and Fitzgerald [38].

2.2 Advances in AFT methodology and data interpretation

The conventional AFT analytical method has been the external detector method (EDM), which uses [nuclear] reactor-induced fission in a low-U muscovite detector as a proxy for apatite ^{238}U content [25, 39, 19]. Alternatively, laser-ablation inductively coupled plasma mass spectrometry (LA-ICP-MS) allows for the direct measurement of U for AFT dating [40]. The LA-ICP-MS AFT method also allows simultaneous acquisition of U-Pb apatite ages ('double dating') and the collection of major and minor trace-element data [41, 42].

One of the more impactful recent improvements in AFT methodology is taking advantage of the faster LA-ICP-MS approach to generate larger numbers of grain ages and utilizing apatite chemical composition during modelling and interpretation. Combining AFT age and length measurements with apatite composition allows the user to identify discrete, statistically viable age populations that have varied compositionally regulated thermal-annealing responses [43, 44]. 'Multikinetic' fission-track behaviour [e.g., 43, 45] is expressed by differences in track annealing between single grains and is common in detrital samples with variable sedimentary provenance or, more generally, from rocks with variable apatite chemical composition. Departures from typical fluorapatite composition (i.e., end-member fluorapatite or hydroxyapatite) are typically characterized by lower thermal-annealing resistance, whereas Cl-rich apatite has long been recognized as being more retentive and resistant to annealing [e.g., 28, 34, 36]. The acquisition of chemical data for AFT grains allows for better defined kinetic-behaviour estimates for use in thermal-history modelling.

The multikinetic AFT interpretation method of Issler et al. [44] is used here and a more detailed description of the various procedures are provided below. At the GSC, electron probe microanalysis (EPMA) is routinely employed for characterizing the composition of the same apatite grains that have undergone AFT analysis. Fluorine, Cl, or OH reside in the apatite anion site; however, OH is not easily measured because ICP-MS methods of collecting elemental data cannot easily measure F, therefore precluding OH estimation. As EPMA can measure F and Cl, these are then used to determine OH by difference. Elements such as F, Na, Mg, P, S, Si, Cl, Ca, Mn, Fe, Sr, Y, La, and Ce are measured by EPMA and reported as weight-percent that are then converted into weight-percent oxide (OH estimation) and atoms per formula unit (apfu), assuming typical end-member apatite stoichiometry using the method of Ketcham [46]; details on this workflow applied to crystalline basement rocks can be found in McDannell et al. [16]. The outcome of the multikinetic approach is that the thermal sensitivity of the sample is

expanded (when compared to modelling all grains as a homogeneous, single population) for samples that demonstrate high single-grain age dispersion and express a relationship between age and composition. In other words, one sample may represent several thermochronometers that can be modelled independently. The implications for modelling are that multikinetic AFT behaviour narrows the possibilities of thermal-history solutions that satisfy the FT data for all grain-age populations from a single sample during simultaneous thermal-history modelling [43, 47, 16, 45]. A single sample may contain between two to four resolvable kinetic populations ranging in thermal sensitivity from under 70 °C to over 200 °C [44], extending the temperature range of the modelled thermal histories beyond the canonical '100–110 °C' quoted in most AFT studies—which often employ a mono-compositional scheme and assume a typical fluorapatite composition [48].

2.3 *AFT interpretation: age dispersion, elemental data, and kinetic parameters*

A radial plot can be used to assess and visualize single-grain AFT age precision and the 'component' ages within a finite mixture [49, 50]. The χ^2 (chi-squared) test is often applied to single-grain AFT ages (and errors) to assess whether grains comprise a single statistically significant population $(P)\chi^2 > 0.05$, or multiple discrete age populations [51]. However, in the case of compositional heterogeneity or grains that have experienced slow cooling through the partial annealing zone, a χ^2 failure may be the rule and not the exception. In the past, most AFT studies utilized 20 (or fewer) age grains and 100 length measurements using the EDM, usually assuming a single statistical population. Samples that failed χ^2 were often still modelled as a single population [e.g., 52] because there were no easily implemented ways of separating age populations using kinetic parameters to improve thermal-history models.

There are also analyst biases associated with the EDM that potentially distort the results of AFT analyses if care is not taken, such as scanning grain mounts for the 'best' grains for measurement [19] or manipulating N_s/N_i ratios (i.e., number of tracks per unit volume relative to number of induced tracks) during sequential FT counting to produce statistically coherent single-grain age populations that pass the χ^2 test [53]. Cratonic basement samples are problematic because they are assumed to contain a single population based on sole apatite source with presumably high spontaneous (N_s) track densities due to either high U and/or old age. In this case, preferential selection of low-N_s grains can occur because they are easier to count, or alternatively, only a few N_s tracks are counted per unit area rather than all observable tracks, which translates to large single-grain age errors. These procedures can produce a single viable statistical population and a central AFT age that is more or less representative of the sample's thermal history; however, these practices may also falsely conceal higher grain-age dispersion and potential effects of radiation-enhanced annealing (REA) on old apatite grains that have resided at low temperatures (< 60–100 °C) for hundreds of millions of years [54, 55]. The existence and nature of REA are debated [13, 56], but are empirically supported by radiation-damage studies [57, 58, 59] and annealing experiments on natural and synthetic apatite [60, 61, 62]. However, comprehensive experiments have yet to be carried out to assess or characterize REA in terms of FT-α-recoil interactions or time-scale dependence.

The LA-ICP-MS AFT methodology is preferred over the EDM due to the above-mentioned analytical benefits and the reduction of analyst bias. Combining LA-ICP-MS AFT with EPMA provides complementary temporal and kinetic data for use in thermal-history analysis. Routine characterization of apatite elemental composition is also extremely beneficial for use in AFT-data interpretation [44]. The AFT grain ages are first evaluated and visualized with radial plots [49] and then mixture modelling is performed on measured AFT grain ages to identify all statistical age populations [63, 64]. This information is used with the accompanying elemental chemistry to identify intrasample kinetic populations of grains of similar age and apatite composition; and to assign measured track lengths to their respective populations based on their measured composition. The identification of 'replicate' EPMA grains is also useful in assessing intragrain heterogeneity and reproducibility [44]. For example, an apatite grain may have been probed once because it was used to calculate an age and that same grain was probed again because it also had length measurements collected from it separately, thus resulting in two probe measurements and directly tying those lengths to the calculated age grain. Assessment of replicate analyses using EPMA typically suggests that intragrain compositional variability is not a problem for most samples [44].

The number of grains analyzed is an underappreciated facet of AFT analysis that has implications for detecting the presence or absence of AFT age populations since the power of statistical tests like χ^2 increase with sample size [65, 66], making it more difficult to pass the statistical test when there are outliers in large and/or precise data sets; similar statistical discussion regarding thermal-history modelling can be found in Vermeesch and Tian [67]. The maximum possible number of single grains should be analyzed for a single AFT sample (e.g., > 20 to > 35) to determine the presence or absence of multiple age populations [55]. Experience has shown that in general, crystalline bedrock samples with at least 30–40 grains, higher LA-ICP-MS AFT age precision, and roughly less than 20–25% age dispersion, are assumed to be a single kinetic population, whereas samples with more than 25–30% age dispersion are usually multikinetic. Mixture modelling may still identify multiple populations in high dispersion cases and produce χ^2 failures, but it is up to the user to determine if viable populations exist based on interpreting the AFT age and length data with compositional information [66].

Electron probe microanalysis elemental chemistry is used to calculate the kinetic parameter r_{mr0} using the established relationship between fission-track retentivity and apatite composition [34, 68]. The r_{mr0} parameter was empirically derived from a set of compositional variables (multivariate equation) determined from analysis using EPMA and annealing experiments on characterized apatite grains. Visualizing potential relationships between ages, lengths, and kinetic parameter is unwieldy when using r_{mr0} because it is nonlinear. Therefore, all r_{mr0} values are converted to a linear 'effective Cl' (eCl) value for comparison to the commonly used kinetic parameter, measured Cl (wt.% or apfu). In other words, eCl values are recast as if they are 'measured Cl' using the r_{mr0}-Cl relation provided in Ketcham et al. [68]. The r_{mr0}-Cl relationship expressed in Ketcham et al.

[68] is:

$$1 - exp(2.107 * [1 - abs(Cl - 1)] - 1.834) \quad (1)$$

Negative eCl values ($r_{mr0} > 0.84$) are indicative of apatite that is lower FT retentivity than the end-member fluorapatite characterized in the Carlson et al. [34] annealing experiments and Ketcham et al. [68] model derivation. The r_{mr0} to eCl conversion is used for data interpretation and then the eCl values are converted back to r_{mr0} for thermal-history modelling. The r_{mr0} (eCl) kinetic parameter has been found to provide the best population discrimination and resolution for AFT data through examination of a large data set of more than 350 duplicate analyses [44, 69]. Approximately 84% of eCl data are reproducible within approximately 0.03 apfu (similar for measured Cl), whereas about 90% of D_{par} (diameter of etched spontaneous fission tracks measured parallel to the crystallographic c-axis) values are within approximately 0.5 μm. These results suggest that measured D_{par} is inadequate for separating kinetic populations due to its lower resolution. In addition, the sole use of measured Cl as a kinetic proxy does not account for cation substitutions or OH (difference of 0.06–0.4 apfu for 40% of analyzed replicates), which produces a significant difference in annealing temperatures that can be upwards of 100 °C if these other elements are not accounted for [44, 69].

The 'improved' annealing model of Ketcham et al. [70] differs from the 1999 model mainly by inclusion of the Cl-dominated apatite data set from Barbarand et al. [35], which revises the data fit and thus the annealing model. Experience has shown that the Ketcham et al. [70] equation narrows the total range of r_{mr0}, making the definition of kinetic boundaries or grouping of grains by composition more difficult. Therefore, use of the Ketcham et al. [68] model, which encompasses a wider range of apatite chemistry without the undue influence of a particular apatite composition, is preferred. The discrepancies between model fits highlight the pressing need for further broad sampling of apatite compositions and additional annealing experiments to refine AFT annealing behaviour. The difference between these models also reveals that the derived kinetic r_{mr0} value is not absolute and can even vary depending on the number of elements measured by EPMA. Consequently, age populations defined by elemental data may require some adjustment during data interpretation and modelling, especially when encountering grains of exotic composition that may not be well characterized by the aforementioned annealing experiments. Assigning lower-than-calculated r_{mr0} values (i.e., more positive eCl values) for extremely retentive populations is often necessary. Grain-age populations with FT retentivity lower than common fluorapatite also must be shifted to greater r_{mr0} values (i.e., more negative eCl values) due to the aforementioned annealing-model misfits. An important clarification is that kinetic populations that are the most chemically similar to the experimentally determined data (e.g., fluorapatite composition) are often well characterized and their r_{mr0} values do not require adjustment. In these cases, the arithmetic mean eCl/r_{mr0} value is used during modelling, or a representative kinetic value is assigned within the sampled range of chemistry for that population. The better-determined 'fluorapatite' population kinetic value is held fixed for modelling, whereas the other end-member populations are adjusted with respect to the well-characterized population.

The AFT samples that exhibit multikinetic characteristics are split up into appropriate age/composition populations and are modelled simultaneously. Thermal histories are generated using computational software of the user's choosing, depending on the preferred statistical approach (i.e., Frequentist vs. Bayesian) and/or the inclusion of multiple thermochronometers.

2.4 *Thermal-history modelling*

Several software tools are available to invert AFT data for thermal histories, including AFTINV [71], HeFTy [72], and QTQt [73]. In this study, inverse thermal-history models are generated using QTQt and AFTINV. These programs employ the same general principles but different statistical frameworks and inverse-modelling approaches. Samples with AFT and other thermochronometer data (e.g., AHe) were modelled using the QTQt software. The inversion scheme implements a Bayesian reversible jump Markov chain Monte Carlo (rjMCMC) routine for thermal-history generation, in which the complexity of the thermal-history solutions is inferred from the data rather than being defined a priori. The Bayesian approach naturally prefers simpler thermal-history models that provide an adequate fit to the observations, rather than more complex histories (that may/may not provide better fits). The rjMCMC routine approach is a learning type of Bayesian algorithm that samples from probability distributions, in which temperature-time (T–t) points are iteratively sampled to construct and refine a continuous thermal history by linear interpolation between sampled points that provide the best fit to the observed data. This is done by first initiating a 'burn-in' period of the model run, where an initial exploration of the model space is performed and subsequently discarded, followed by the post-burn-in phase, which is used to estimate the posterior distribution for the model parameters. Thermal-history construction begins by initializing a T–t search space (prior; i.e., essentially a 'guess' about an uncertain probability distribution without accounting for any data) to generate a discrete series of T–t points, assuming a uniform distribution for temperature (e.g., between 0 and 200 °C) and time (e.g., between 0 and 1000 Ma). The time and temperature points (initial/current history) are perturbed many times (proposed model) either by removing a random T–t point (death) between two adjacent points or by introducing a new point randomly, then interpolating between adjacent points and introducing a T–t perturbation [(birth; see Fig. 1 of 73]. If a better fit is found during perturbation, then the model T–t path is adjusted to the newer, better fit; however, if a poorer-fitting history results from the T–t perturbation(s), then the process can return to the previous node and/or iterate until a better fit is found. The model output is an ensemble of thermal histories that quantify the range of accepted models in terms of a posterior probability distribution. Primary QTQt-model outputs include three time-temperature models that we focus on here:

- The maximum likelihood (ML) model is the model that fits the measured data the best but is the most complex.
- The maximum posterior (MP) model is the simplest model, where the posterior probability is proportional to the likelihood multiplied by the prior (no uncertainties are associated with the MP or the ML models).
- The expected (EX) model is essentially a weighted-mean model of intermediate complexity between the ML and MP

models, where the weighting is provided by the posterior probability of each model solution. The iterative MCMC sampling can be used to calculate the uncertainty for the EX model and define the 95% credible interval (CI; Bayesian equivalent to the confidence interval) around the EX-model solution.

The ML and MP models will be the same in cases of constant dimension (i.e., number of T–t points) and for uniform prior distributions applied in QTQt. The distinction is that QTQt uses transdimensional rjMCMC sampling, where the number of T–t points are free to vary, so the prior penalizes the model if it becomes too complex; therefore, the MP model will normally be simpler (less T–t points) than the ML model. The MP model is sensitive to the range of the prior specified for the general thermal-history model; the larger the time span of the prior, the more the posterior models tend to be simple. This can be a cause for concern when justifying (or inferring) more complex histories for models spanning long time intervals with few thermochronometric data [48].

The QTQt software allows resampling of thermochronometric ages, commonly by assuming a normal distribution (the standard deviation) centred on the measured radiometric age (N_s/N_i ratio for AFT), or alternatively, resampling of the chosen kinetic parameter (i.e., measured Cl value ±), which is a way of recognizing uncertainty in laboratory-calibrated kinetic models extrapolated to geological time scales. The primary QTQt modelling parameters that are used here are the Ketcham et al. [68] annealing algorithm, the eCl/r_{mr0} (eCl) kinetic parameter, and c-axis projected FT lengths.

The AFTINV software [71] employs a nondirected random Monte Carlo search algorithm and p value thresholds as goodness-of-fit (GOF) objective-function criteria for fitting observed AFT central or pooled ages and track-length distributions—similar to the commonly used HeFTy software [72]. The AFTINV software was developed from the model of Willett [74] to model more complicated thermal histories and multikinetic AFT annealing [71, 43]. Thermal histories are generated on a time-temperature grid by random selection of heating and cooling rates within prescribed limits per time step, subject to available geological constraints such as depositional age or timing of an unconformity. The model is run until a predetermined number of statistically acceptable solutions are obtained; the exponential mean of these solutions usually provides a smoothed, representative, good-fitting solution. The overall minimum objective-function solution (best-fit) is defined as either the lowest combined objective function for AFT age, length, and %Ro (the default) or the lowest maximum objective function (age, length, or %Ro). The model allows for ten different thermal-history styles that can be used individually or in combination to generate complicated thermal histories, with multiple thermal minima and maxima over variable time and temperature ranges. The random Monte Carlo (MC) solution set determined for the 0.05 significance level (e.g., 300 solutions at the 0.05 level) can be used as a 'seed' history pool for the controlled random search (CRS) algorithm [75, 74] to improve or refine the 0.05 solution set to the 0.5 level. The CRS algorithm is a learning algorithm that takes an ensemble of randomly generated T–t histories and creates new histories in the same neighbourhood as the current pool, compares the objective-function fit to the observed data, and iteratively replaces the worst fitting solutions with better solutions. The model converges when all solutions exceed the 0.5 threshold or when it cannot improve the solution set after a fixed number of iterations. The tactic of using the 0.05 random MC solutions as a seed pool for the CRS algorithm reduces the (potential) problem of becoming trapped in a local minimum and converging on too narrow a region of solution space. This circumvents the normal approach of initiating the CRS algorithm by generating a random set of solutions that may or may not provide any reasonable fits to the data. The latter issue of a random starting pool can be problematic (especially over long timescale models) because the CRS algorithm may identify a 'good-fitting' region of T–t space and begin focusing on improving solutions without fully searching the model space. The CRS approach is described thoroughly in Willett [74], Harrison et al. [76], McDannell [15], McDannell et al. [8, 16], and McDannell and Flowers [18]. The most current AFTINV modelling approaches are discussed in Powell et al. [47, 77], McDannell et al. [16], and Schneider and Issler [45].

3 OVERVIEW OF AFT DATA IN CANADA

A recent compilation of AFT analyses in Canada includes 1138 analyses based on the population, EDM, or LA-ICP-MS methods, with around 20% of samples collected from wells or underground mines (Fig. 1; [78]). The distribution of AFT analyses is highly irregular, with British Columbia accounting for 36% of the data set. In contrast, large portions of the Canadian Shield are underrepresented or absent from the data set. Published data sets vary significantly in quality and rarely include individual grain-age results, length data, and one or more kinetic parameter(s), making the data extremely difficult to interpret or reuse. This is especially an issue with pre-2000s vintage data. Twenty-three percent of compiled results have grain-age data and most do not include apatite-grain geochemistry. The lack of detailed and complete analyses in most of the samples from the Canadian Shield prevents a fair appraisal of individual analyses or general assumptions about regional trends.

Most fission-track ages across the Canadian continental interior are Paleozoic to Mesozoic and reflect varying degrees of burial by sedimentary strata in the Phanerozoic. A preliminary map source and reference list for most of previous fission-track studies undertaken in Canada can be found in Pinet and Brake [78]. References to some of the relevant applied studies in the Canadian interior and the Arctic include: Issler et al. [79]; Naeser and Crowley [80]; Crowley [81]; Ravenhurst et al. [82]; Arne et al. [83]; Issler et al. [84]; Osadetz et al. [85]; Lorencak [86]; Lorencak et al. [87]; Grist and Zentilli [88]; Issler et al. [43]; Kohn et al. [89]; Issler and Grist [90]; Feinstein et al. [91]; McGregor et al. [92]; Pinet et al. [93]; Issler et al. [44]; Powell et al. [47, 77]; McDannell et al. [16, 55]; and Schneider and Issler [45].

4 TRANS-ARCTIC APATITE FISSION-TRACK DATA FROM GEM-2

The regional-scale interpretation of AFT and AHe data sets is underway and will be released when completed (see Fig. 2A). Newly acquired AFT data from two samples collected on

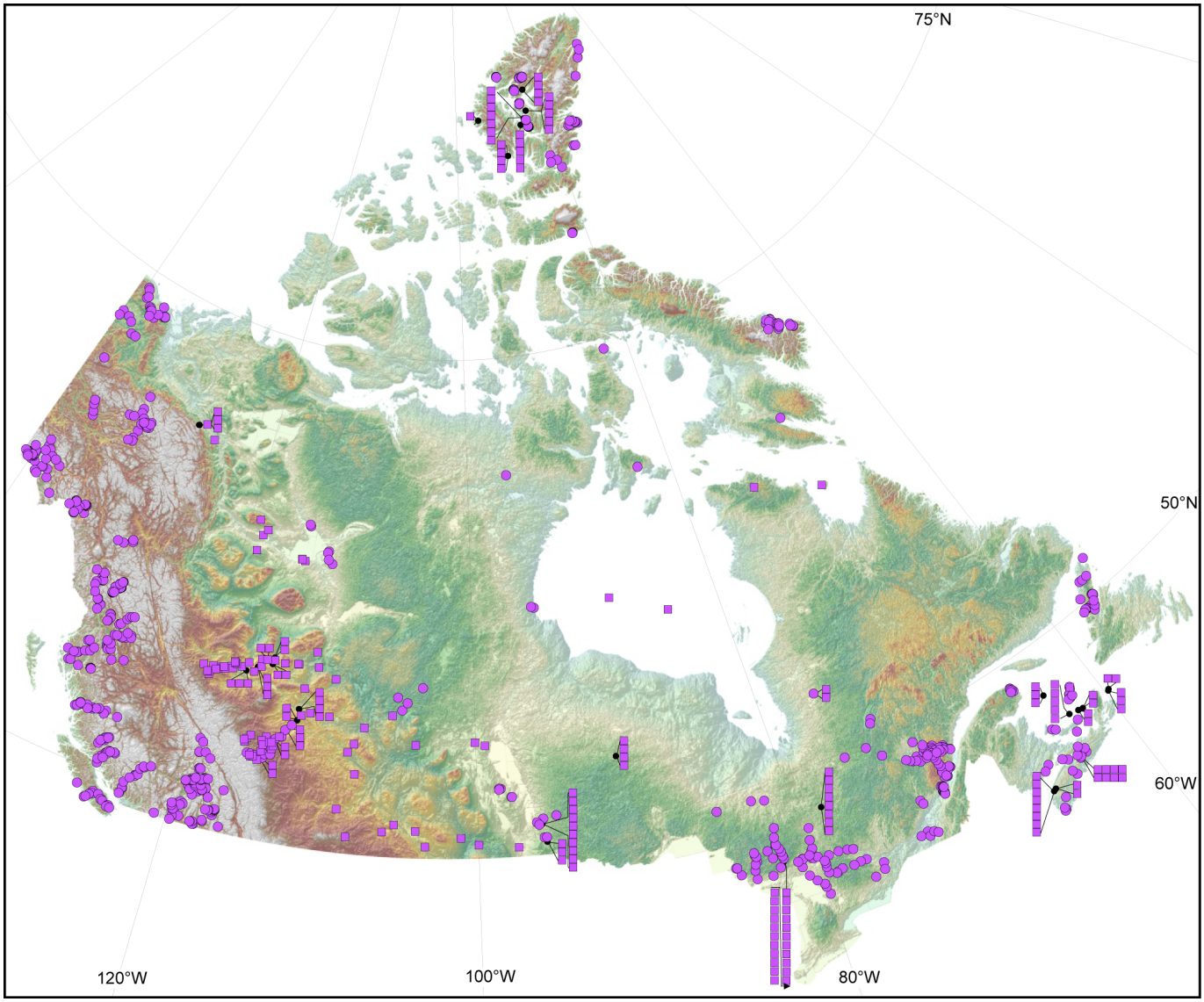

Figure 1: Location of published/available apatite fission-track analyses in Canada, compiled by Pinet and Brake [78]. Circles correspond to surface samples and squares are from mines and/or boreholes. More comprehensive information and data sources can be found in Pinet and Brake [78].

Southampton Island, in Nunavut, are discussed below and are an example in which the preserved sedimentary succession provides a geological constraint on thermal conditions during the Late Ordovician–early Silurian. This example also allows the comparison of inverse-modelling results with other tools used in previous studies to constrain the thermal evolution of the area and provides the opportunity to critically assess common analytical procedures (e.g., number of apatite grains analyzed or geochemical variations) and different modelling strategies (e.g., multikinetic approach or software choice). A crystalline basement sample from northern Ontario collected 50 km from the Paleozoic unconformity exemplifies the case in which a relatively high-temperature constraint is used to infer the pre-Paleozoic thermal history above the partial annealing zone for fission tracks in apatite (~60–110 °C). The AFT analytical procedures are discussed in Appendix 8.

4.1 Sample locations

Samples for AFT and EPMA were mainly collected from the GSC geochronology mineral-separate archive in Ottawa, and some were rocks obtained from research scientists in the Ottawa offices of the GSC or from external research organizations such as provincial geological surveys, and mining industry rock cores (e.g., DeBeers Canada). Figure 2A shows the distribution of GEM-2 AFT samples from Archean–Paleoproterozoic crystalline bedrock (various lithologies) across the Canadian Shield and the Arctic Islands. The low-temperature thermochronometry data for these samples compliment previous large, regional thermochronology studies carried out in Canada; namely, southern Ontario samples dated via AFT by Lorencak [86] and summarized in Kohn et al. [89], and the northwestern Canadian Shield (i.e., Slave Craton and East Lake Athabasca region) samples dated by AFT and AHe [5, 14, 94]. The data from Lavoie et al. [95] and Pinet et al. [93] are shown, some of which are remodelled and summarized in the results for Southampton Island and the Hudson Bay region discussed below. Some of the AFT samples dated during the GEM-2 program are thoroughly discussed in McDannell et al. [55], whereas sample 12RM086 from northern Ontario is presented here for the first time. The AFT data set for most of the GEM-2 project is available in the Mendeley Data repository [96], a product developed by Elsevier.

4.2 Southampton Island, Nunavut

4.2.1 Geological setting and previous thermal indicators

On Southampton Island, the preserved Paleozoic sedimentary succession (Fig. 2B) consists mainly of carbonates formed in shallow marine conditions during the Late Ordovician to early Silurian [98, 99, 100]. The succession is nearly flat lying (see Fig. 3A), although the contact with the crystalline basement is often marked by steeply dipping faults with generally minor offsets of 10 m or less [98]. Steeply dipping faults near the northeastern shore (Fig. 3B) may belong to a (mainly) offshore fault system. This fault system records an extensional (or transtensional) tectonic event of poorly constrained age that resulted in the formation of subbasins with the geometry of a half-graben [101, 102].

The thermal history of the Paleozoic succession on Southampton Island has been recently investigated using multiple organic-matter and mineral-based tools that yielded conflicting results [103]:

- Rock-Eval 6 analysis of outcrop samples indicated that they are immature (T_{max} values lower than 435 °C for samples with S_2 greater than 0.35 mg HC/g rock; [95]).
- Reflectance petrography of Ordovician oil-shale outcrop samples (Red Head Rapids Formation) indicated that organic matter Ro-equivalent values vary from 0.48 to 0.55% [104, 95], confirming that these source rocks are immature.
- Inverse modelling of AFT analysis from one Ordovician basal sandstone sample reported in Pinet et al. [93] suggested maximal burial temperatures between 65 and 85 °C, suggestive of early mature conditions.
- Microthermometry of fluid inclusions from an Upper Ordovician reefal build-up showed that recrystallized early synsedimentary cements were characterized by high homogenization temperatures (average Th of 117.9 ± 25 °C), whereas late calcite cements corresponded to lower entrapment temperatures (average Th of 92.6 ± 9.7 °C); both the early and late cements suggested mature conditions.
- Preliminary carbonate clumped-isotope thermometry analyses on samples from the same Ordovician reef analyzed for fluid inclusions yielded temperatures ranging from 26 to 46 °C for late cements and 41 to 66 °C for replacements of early cements.

Each of the methods used to constrain the temperature maxima or range in temperatures experienced by the samples have their own drawbacks and, perhaps more importantly, their own spatial and temporal scales. Organic matter-based methods, which are the most commonly used in sedimentary basins, may be affected by external factors such as organic facies, temperature and pressure, and/or suppression phenomena [105]; in addition, these methods only constrain the peak temperature. On Southampton Island, published AFT data [95, 93] came from an Ordovician sandstone sample and had only 15 apatite grains, which is probably not enough to fully characterize the sample in terms of potential detrital apatite single-grain age and chemical variation (see below).

In some cases, fluid inclusions can be reset (i.e., secondary fluid inclusions) when primary fluid inclusions are altered during a later heating event. Calcite crystals are particularly prone to alteration and great care should be taken when gathering data. The higher temperatures found in early cements for the Southampton samples strongly suggested a hydrothermal event of limited scale altered the signal of the primary fluid inclusions. Clumped-isotope thermometry results may be associated with mineral crystallization but can also be affected by the amount of recrystallization/alteration at various stages of the thermal evolution (including some solid-state reordering at high temperatures) or contain Δ47 values locked at closing temperatures during cooling [103].

4.2.2 Northern Ontario, Hudson Bay region

The Paleozoic, which may or may not include Mesozoic and minor Cenozoic [e.g., 106], rocks situated along southern Hudson Bay overlie Archean basement of the western Superior Province and Trans-Hudson Orogen, reaching sedimentary thicknesses

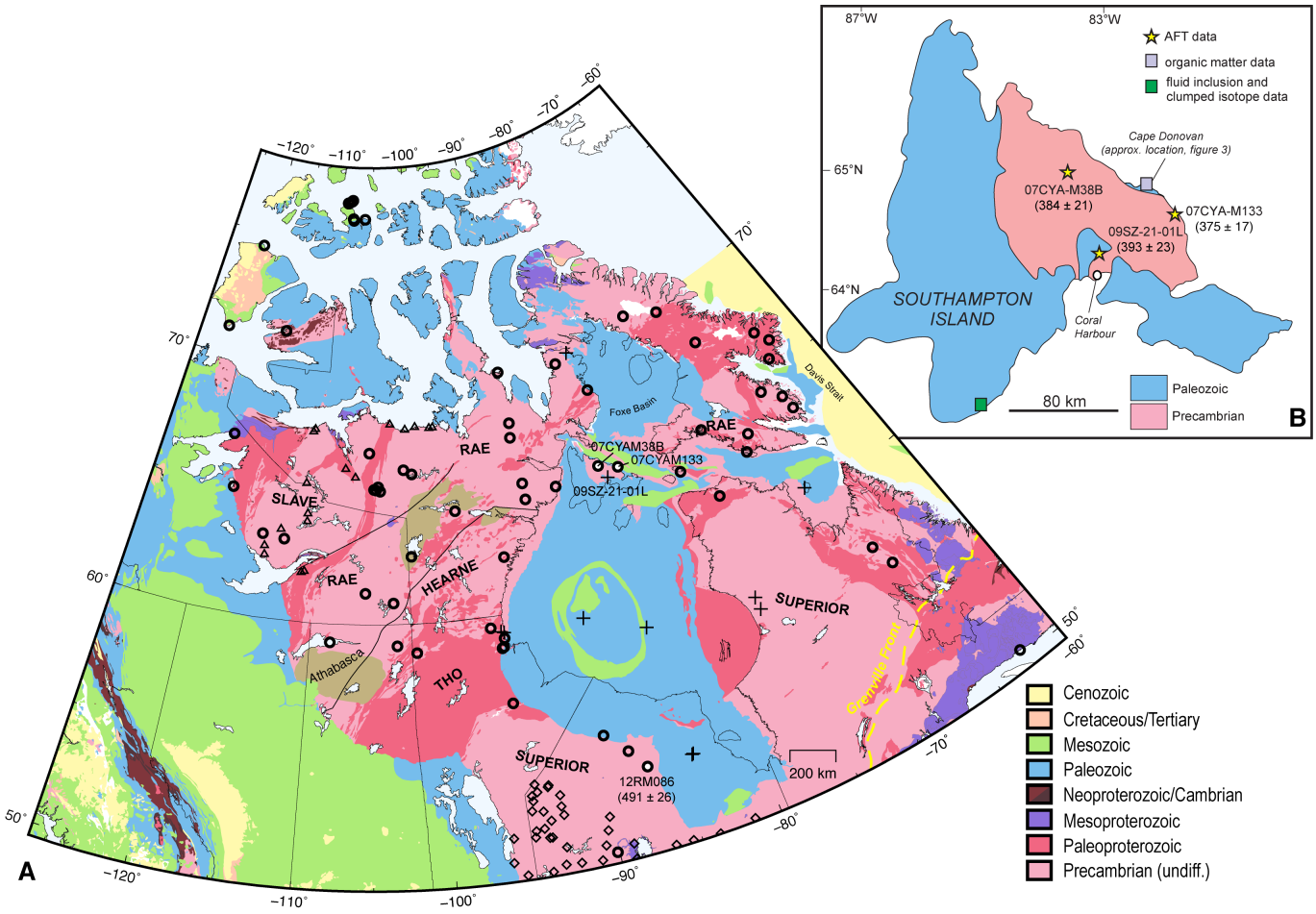

Figure 2: **(A)** Location of GEM-2 thermochronology samples (circles). Other regional apatite fission-track (AFT) and AHe studies of the Hudson Bay region are also shown (diamonds for Lorencak [86] and Kohn et al. [89]; triangles for Ault et al. [94]; crosses for Lavoie et al. [95] and Pinet et al. [93]). Southampton Island and Ontario samples discussed in the text are labelled. Geology simplified from Wheeler et al. [97]. All major cratonic domains of the Canadian Shield are labelled, along with the Paleoproterozoic ca. 1.7 Ga Athabasca and Thelon basins (brown), and Trans-Hudson Orogen (THO; dark red). Note: offshore geology is not shown in the Arctic Islands, whereas the Paleozoic through Cenozoic rocks are shown for Hudson Bay, Hudson Strait, Foxe Basin, and Davis Strait offshore Baffin Island to demonstrate the extent of onshore-offshore continuity. **(B)** Simplified geology of Southampton Island, Nunavut, showing location of AFT, organic maturity, and fluid-inclusion samples. Central AFT ages calculated at 1σ.

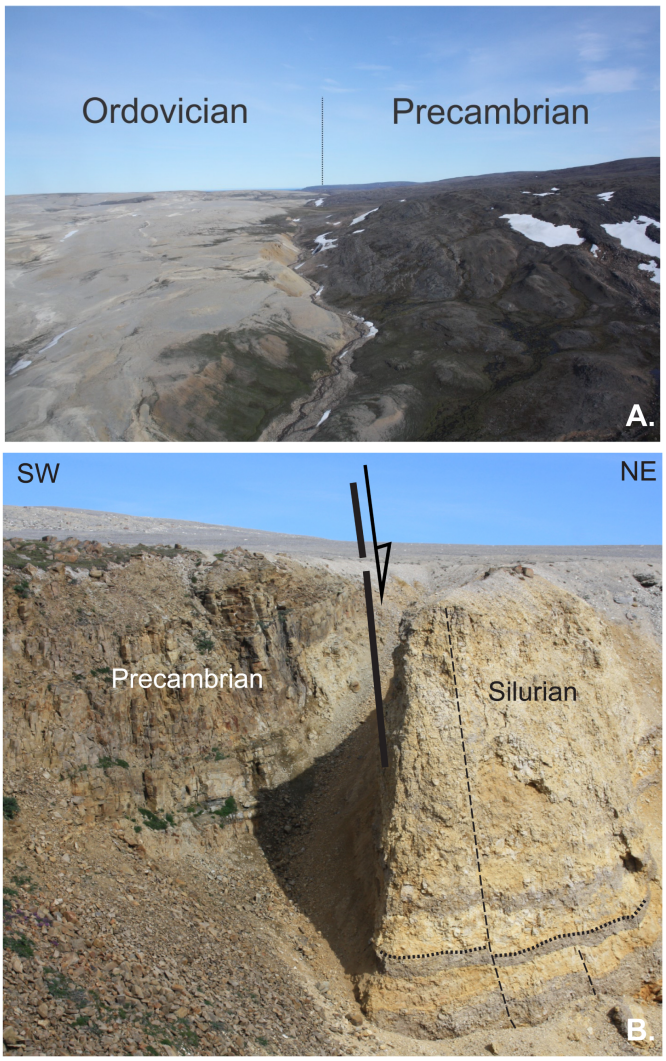

Figure 3: **(A)** Aerial view showing the shallow-dipping Precambrian–Paleozoic (Ordovician) contact on Southampton Island, Nunavut. Photograph by N. Pinet. NRCan photo 2019-530. **(B)** Steeply dipping fault juxtaposing Silurian rocks against Precambrian basement near Cape Donovan, on the northeastern shore of Southampton Island. Photograph by N. Pinet. NRCan photo 2019-529.

of a few hundred metres onshore [107, 108, 109, 110, 95, 101], and over 2000 m beneath Hudson Bay (Fig. 4; [e.g., 101]). In both the Hudson Bay Basin and Moose River Basin, the base of the sedimentary succession is the Upper Ordovician (ca. 450 Ma) Bad Cache Rapids Formation [99, 111, 112]. These basins are separated by the Cape Henrietta Maria Arch (or Transcontinental Arch of Sanford [109]), a physiographic element that acted as a positive topographic feature and influenced deposition during the Paleozoic.

Sedimentary rocks are mainly Ordovician through Devonian (Fig. 4; also see Lavoie et al. [103]). The succession was deposited in relatively shallow marine environments and consists mainly of limestone, dolostone, and evaporite with only minor amounts of sandstone and shale. The subsidence history is irregular and several unconformities have been documented in the Ordovician to Devonian succession [101]. Among these unconformities, the one located close to the Early–Middle Devonian boundary divides the succession into two main sedimentary packages: a lower package cut by high-angle faults and an essentially nondeformed upper package. Significant changes in the Hudson Bay Basin depocentre location during the Paleozoic have been interpreted based on vintage, poor-quality seismic data [101].

The tectonic subsidence curve for the Hudson Bay Basin does not exhibit the low subsidence tail that characterizes many intracratonic basins, suggesting that the upper part of the succession has been removed by erosion [101]. The late- to post-Paleozoic history of the Hudson Bay region is poorly constrained. The presence of marine Pennsylvanian rocks in Hudson Bay has been suggested by Tillement et al. [115], but remains controversial. In the James Bay lowlands (Moose River Basin), there is a thin interval of Middle Jurassic (ca. 170 Ma) Mistuskwia Beds [108] overlain by the Cretaceous Mattagami Formation, dated at ca. 112 to 97 Ma [116], that was deposited in a shallow marine setting that may have been more regionally widespread [117]. Flooding and burial of the North American interior occurred during high sea-level stand, creating the Cretaceous Western Interior Seaway [118, 119, 120]. Stratigraphic evidence for an unconformity of about 110 to 100 Ma is documented across a broad area of northern and western Canada [121] but is poorly documented in central Canada. There is also support for an Albian 'arm' of the seaway that extended across Hudson Bay (and Southampton Island) and connected Hudson Strait with the opening Atlantic Ocean and Labrador Sea [117].

This Moose River Basin region also hosts Proterozoic (Kyle Lake) and Jurassic (Attawapiskat/Victor) kimberlites [122, 123, 124] that pierce roughly 250 to 300 m of Ordovician through Silurian rocks. The Jurassic kimberlites were emplaced at a depth of about 600 m [125], implying minor (± 350 m) subaerial erosion since the Jurassic; it is presently unclear whether this near-surface constraint is only local or more regional in nature.

The low-temperature thermal history of the southwestern edge of the Hudson Bay Basin is poorly constrained. The T_{max} and organic matter Ro-equivalent values for outcrop and onshore shallow-well samples indicate that they are thermally immature, except for samples from the base of the Comeault #1 well in northeastern Manitoba (Fig. 4) that reached the early oil-generation window [103].

Apatite fission-track sample 12RM086 was collected in northern Ontario, approximately 50 km west of the present-day edge of Paleozoic strata, in an area that was almost devoid of previous AFT characterization (Fig. 2). On a broad scale, an episode of Paleozoic heating ranging approximately between 70 and 100 °C has been documented for Precambrian samples located on the southwestern edge of the Hudson Bay Basin by Crowley [81], Osadetz et al. [85], Lorencak [86], Lorencak et al. [87], Feinstein et al. [91], and Pinet et al. [93]. This compares with inverse-modelling results for samples from the Musselwhite mine in northern Ontario [126], collected approximately 230 km west of sample 12RM086, which indicated that Paleozoic–Mesozoic heating was limited or absent. A Jurassic sandstone collected from the nearby Victor kimberlite mine in James Bay yielded a weighted mean (n = 2) uncorrected apatite (U-Th)/He date

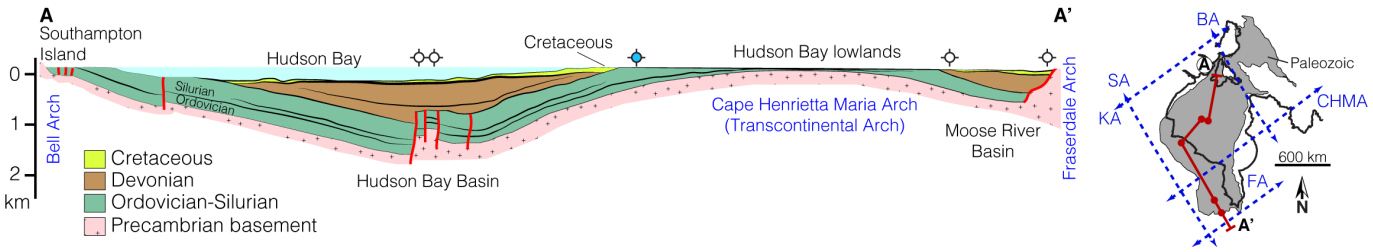

Figure 4: Geological cross-section across Hudson Bay Basin (modified from Norris et al. [113]). The Phanerozoic geology is simplified and coloured according to sequences in Sloss [114]. Red lines are intrabasin faults. Major regional arch structures are shown in the inset as dashed blue lines: Bell Arch (BA); Cape Henrietta Maria Arch (Transcontinental arch) (CHMA); Fraserdale Arch (FA); Keewatin Arch (KA); Severn Arch (SA; trending northwest). The dark red line (A–A' in the cross-section) extends from Southampton Island to the Moose River Basin and the points along the line correspond to drilled exploration wells in the Hudson Bay Basin (Comeault #1 well, in Manitoba, is third from right in the inset and blue dot on cross-section). Gray area in the inset outlines Paleozoic and younger rocks (*see* Pinet et al. [101]).

of 223 ± 34 Ma [95], nearly overlapping with the ca. 180–155 Ma eruption age of the Victor kimberlite field [125]. The pre-Jurassic detrital He dates demonstrate that there was little to no post-Jurassic burial of the Moose River area.

5 THERMOCHRONOLOGY RESULTS

The AFT samples presented first are from Southampton Island. Ordovician sandstone sample 09SZ-21-01L has a central AFT age of 393 ± 23 Ma (1σ), a mean track length (MTL) of 12.3 ± 1.2 μm (n = 51), an average eCl of 0.02 ± 0.02 apfu (r_{mr0} = 0.833), and a measured average D_{par} of 1.6 μm. Apatite (U-Th)/He data were also collected for this sample but were not modelled in Pinet et al. [93]. Corrected apatite He dates (n = 5) range from 334 ± 22 Ma to 577 ± 34 Ma (1σ) with effective U (eU = U + 0.238 * Th + 0.0012 * Sm) values ranging between 5 and 44 ppm (average = 25 ppm). The data exhibit a positive age-eU trend, implying older apparent ages have accumulated greater radiation damage [14, 127]. There is no age correlation with (grain size) equivalent spherical radius. The Gerin et al. [128] vacancy damage ^{4}He diffusion model was used in QTQt and resampling of the 'damage effect' parameter (E_b) was allowed between 20 and 60 kJ/mol, which corresponds to the activation energy (ΔEa) required for ^{4}He to escape a vacancy damage site 'trap' (typical value of ~25 kJ/mol for Durango fluorapatite).

New samples from Southampton Island Precambrian bedrock are a diorite (07CYA-M133) and a gabbroic anorthosite (07CYA-M38B). Sample 07CYA-M133 has an AFT central age of 375 ± 17 Ma (1σ), a mean track length (MTL) of 11.6 ± 2 μm (n = 101), average eCl of -0.097 ± 0.02 apfu (applies to probed age grains only; r_{mr0} = 0.869), and measured average D_{par} of 2.3 μm. Sample 07CYA-M38B has an AFT central age of 384 ± 21 Ma (1σ), a MTL of 12.2 ± 2 μm (n = 132), average eCl of 0.007 ± 0.03 apfu (applies to probed age grains only; r_{mr0} = 0.838), and measured average D_{par} of 1.9 μm.

Figure 5 shows radial plots for the three samples from Southampton Island: the Ordovician sandstone and the Precambrian diorite (Fig. 5A, B, respectively) are characterized by a low number of measured grains (both n = 15) and are statistically indistinguishable, whereas the gabbroic anorthosite in Figure 5C (n = 40) shows the presence of three apparent age populations and much higher dispersion (16–18% vs. 30% for the latter). However, all three samples yielded the same AFT central age (within error). The addition of the 'extra' two populations in Figure 5C shows that this sample has the potential to provide more T–t information than the other two samples. Measured Cl and D_{par} (Fig. 6A) and Cl content (Fig. 6B) are unable to resolve age populations and, although in this case eCl is moderately successful, there is still significant population overlap (Fig. 6B). Sample 07CYA-M38B also displays a negative age-eU trend (Fig. 6D) that is characteristic of REA [55], which makes multikinetic population separation more challenging [16]. The grain-population boundaries are in most cases blurred, rather than sharp and well defined. Therefore, grains are reassigned to populations based on visual inspection of approximate boundaries using both ages and lengths with respect to composition, and subsequently assigned the average eCl value of the overall population (Fig. 7A). Figure 7B demonstrates this process for the AFT lengths—as the boundary between kinetic populations no. 1 and no. 2 falls somewhere between approximately -0.01 and -0.03 apfu (similar boundary for grains on AFT age vs. eCl plot of 6C). The boundary is set at -0.01 apfu (Fig. 7C), because this value requires the reassignment of the least number of both age and length values to grains from their original calculated eCl values.

Sample 12RM086 (northern Ontario) is from a K-feldspar porphyritic quartz monzonite and has an AFT central age of 491 ± 26 Ma (1σ, n = 25), a MTL of 12.7 ± 1.7 μm (n = 130), average eCl of -0.022 ± 0.02 apfu (applies to probed age grains only; r_{mr0} = 0.847), and measured average D_{par} of 2.0 μm (Fig. 8A–D) This sample has three recognized age populations of 361 ± 12 Ma, 548 ± 14 Ma, and 749 ± 38 Ma on a radial plot (Fig. 8A); however, the third population (kin. pop. no. 3; ca. 750 Ma; Fig. 8B) is poorly resolved and overlaps the others in kinetic space. After multikinetic interpretation using grain ages, lengths, and eCl to distinguish age populations (Fig. 8C), the pooled ages for each population were determined to be 358 ± 16 Ma, 547 ± 20 Ma, and 755 ± 272 Ma (large error because of low 'n' and pooled age calculation), in excellent agreement with those recognized from radial plot mixture modelling (Fig. 8B). Figure 8D shows that there is complete overlap between age populations when using D_{par}, further demonstrating that it is inadequate for multikinetic interpretation [e.g., 44, 16, 69].

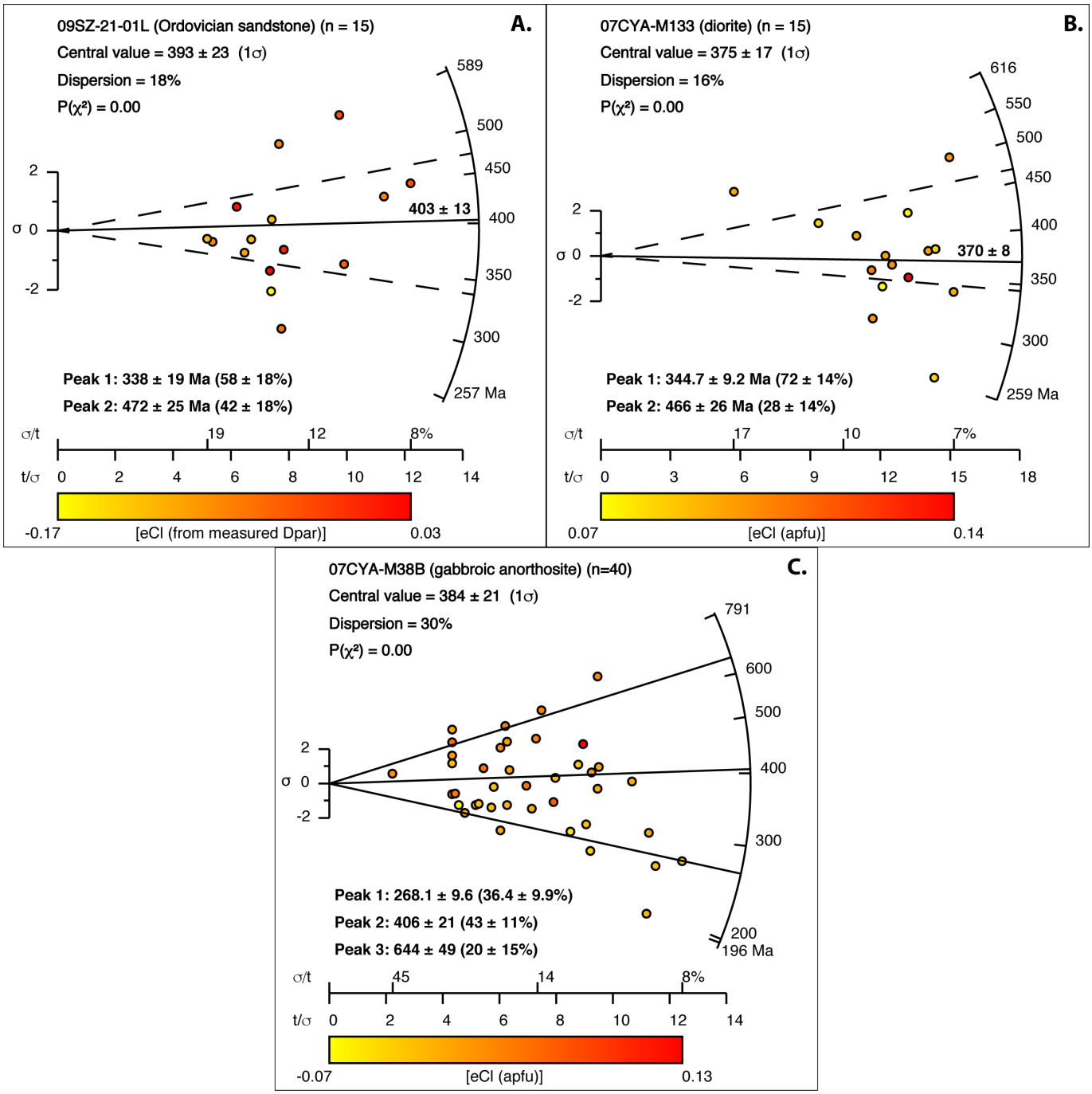

Figure 5: Radial plots for apatite fission-track samples from Southampton Island, Nunavut. **(A)** Ordovician sandstone sample 09SZ-21-01L is reported in Lavoie et al. [95], Pinet et al. [93]. **(B)** Diorite sample 07CYA-M133 and **(C)** gabbroic anorthosite sample 07CYA-M38B are samples from Precambrian basement. Radial plots [49] are a way to visualize single-grain ages and precision and are here coloured by eCl expressed in atoms per formula unit (apfu). Higher grain-age precision is denoted by greater distance from the origin. Grain ages that fall far outside of the 2σ bounds typically lead to χ^2 failure. Age mixture modelling is done in DensityPlotter software v. 8.4 [63, 64] and results in the identified age populations, which are labelled as peaks 1, 2, and 3. Samples in panels **(A)** and **(B)** 'auto' pick two populations but, based on the overall age dispersion (<20%) and the grain chemistry, those populations are unable to be verified with the available data, so only one population is selected for modelling.

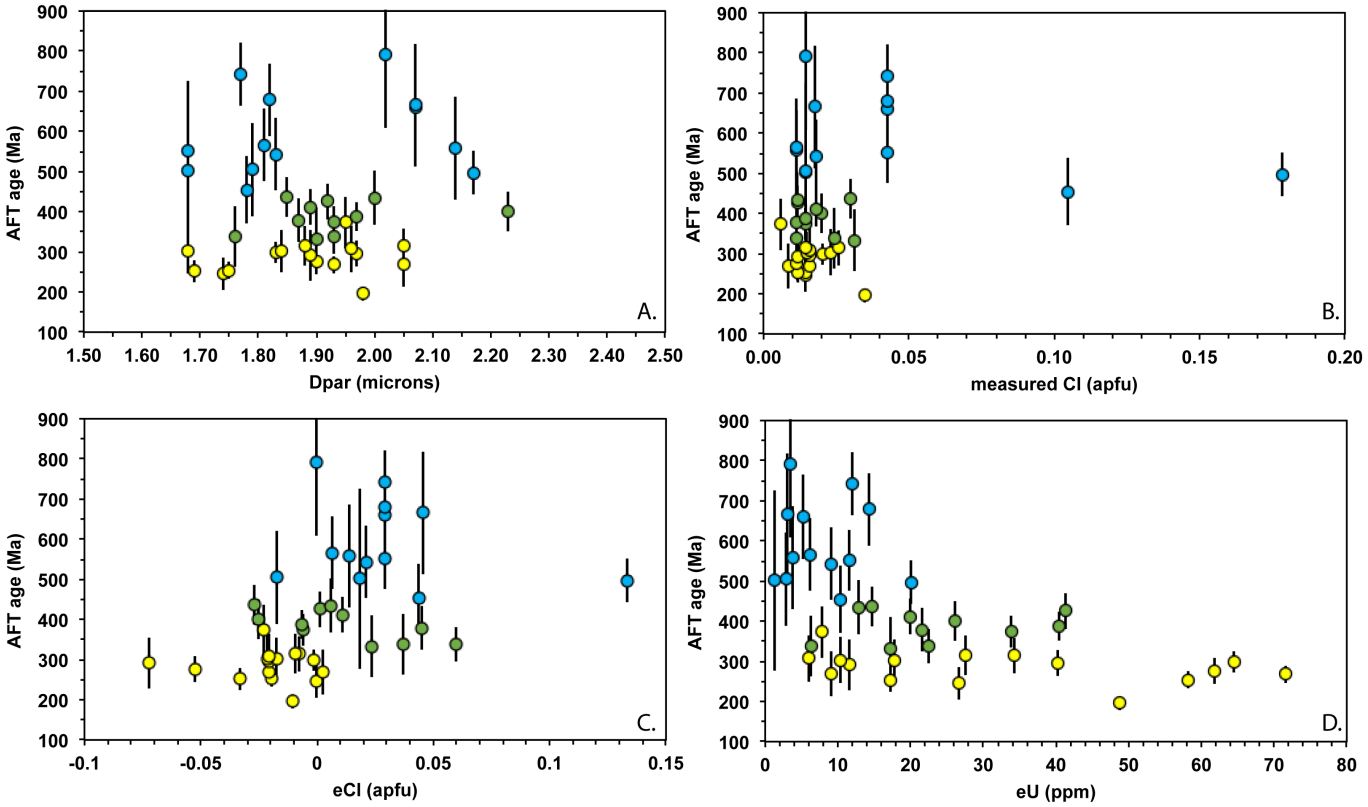

Figure 6: Plots of **(A)** apatite fission-track (AFT) age and Dpar; **(B)** measured Cl, **(C)** eCl, and **(D)** eU for sample 07CYA-M38B from Southampton Island, Nunavut. Population overlap exists for all three populations in kinetic space (kin. pop. no. 1 = yellow; kin. pop. no. 2 = green; kin. pop. no. 3 = blue). Some grains were not probed and are assigned the average eCl value from their respective age population expressed in atoms per formula unit (e.g., kin. pop. no. 3 values at ~0.028 apfu). Effective Cl (eCl) shows the best resolution, albeit with radiation-enhanced annealing effects likely causing the large age scatter given the narrow compositional range, shown in panel d, where grains with old ages have low damage (low eU in parts per million (ppm)) and high eU grains have higher damage accumulation and younger ages.

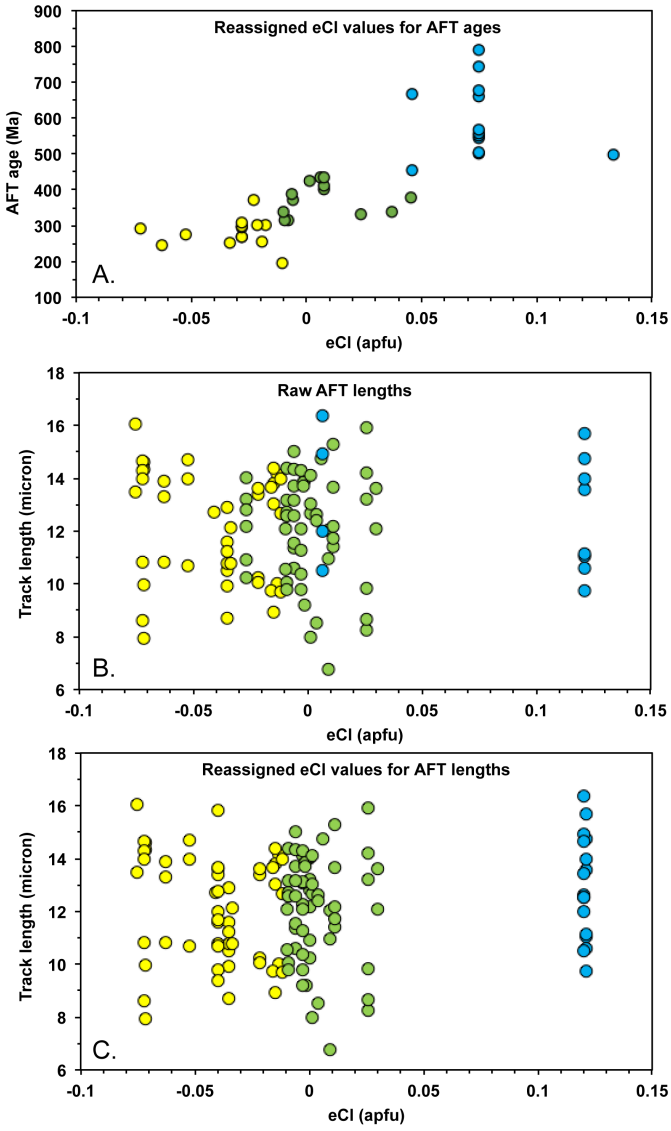

Figure 7: **(A)** Apatite fission-track (AFT) age-grain kinetic population after interpretation and reassignment for thermal-history modelling for sample 07CYA-M38B from Southampton Island, Nunavut. The AFT lengths before **(B)**, and after **(C)**, kinetic population reassignment. Note: there is much less overlap in eCl space (given in atoms per formula unit (apfu)) for kinetic populations plotted against track length. Single-grain age errors not shown for clarity.

6 THERMAL HISTORY RESULTS

Thermal-history results are discussed in the presentation order of the samples, with those having the most thermochronology data and geological constraints described first, followed by samples that were more difficult to interpret (e.g., less geologic information, multiple kinetic populations, or the possible presence of REA), and finally samples with only a single chronometer (AFT data only). Both QTQt and AFTINV software were used to compare different statistical approaches and modelling methodologies for samples from old rocks with protracted thermal histories and limited geological constraints. Overall, the quality of the AFT age data (as indicated by age dispersion and identified radial-plot age populations) is lower compared to the FT-length data; therefore, the choice was made to fit the age data to two standard deviations (0.05 level), while letting the CRS algorithm fit the length data at the 0.5 level in the AFTINV models. An important point to keep in mind is that statistical goodness-of-fit (GOF) values are reported for the AFT central-age and track-length distributions computed during QTQt inversions; however, it should be noted that these are not directly comparable to those in AFTINV (or a similar program like HeFTy). The primary difference is that in AFTINV or HeFTy, the objective/merit-function criteria are used to assess the viability of a particular simulated history with respect to a comparison between the observed and model chronometer data, whereas QTQt does not use GOF criteria to assess histories and instead uses iterative MCMC sampling and a log-likelihood function to produce credible intervals around the EX solution. Moreover, there are no uncertainty estimates associated with the ML or MP model T–t paths. The quoted QTQt GOFs are calculated after the inversion is complete for a particular T–t path (e.g., ML or MP path), thus the value computed for the specific output T–t history is not used during the inversion to assess a particular fit between model and observed data and should be viewed as an approximation only for comparing results from AFTINV and QTQt.

6.1 Southampton Island thermal-history model: sample 09SZ-21-01L

The explicit T–t boundary conditions imposed on the model for sample 09SZ-21-01L are as follows: the maximum allowed heating/cooling rate ($\delta T/\delta t$) is 2 °C/Ma, the prior (initial) T–t space ranges from 850 to 0 Ma and 150 to 0 °C; and the only imposed geological constraints are an Ordovician stratigraphic age of 455 ± 5 Ma at a surface temperature of 20 ± 10 °C and a modern surface temperature of 5 ± 5 °C. Sample 09SZ-21-01L has an AFT central age that is younger than the stratigraphic age, indicating it has been partially annealed. Models are typically run in stages with initial, fast exploratory models of approximately 20 000 to 40 000 total iterations, where 10 000 to 20 000 iterations are discarded during the burn-in phase followed by 10 000 to 20 000 additional models retained in the post-burn-in phase. This allows for the birth/death and T–t acceptance rates to be examined and 'proposal move' values to be adjusted, if necessary, to fine-tune the MCMC sampling and allow the model space to be fully explored during successive run(s) at longer iterations. The models are then run through at least 200 000 to 650 000 or more total iterations to ensure satisfactory convergence and prior-space exploration (ML/MP sampling-chain means are flat). The MCMC acceptance rates for T–t jumps for reported thermal

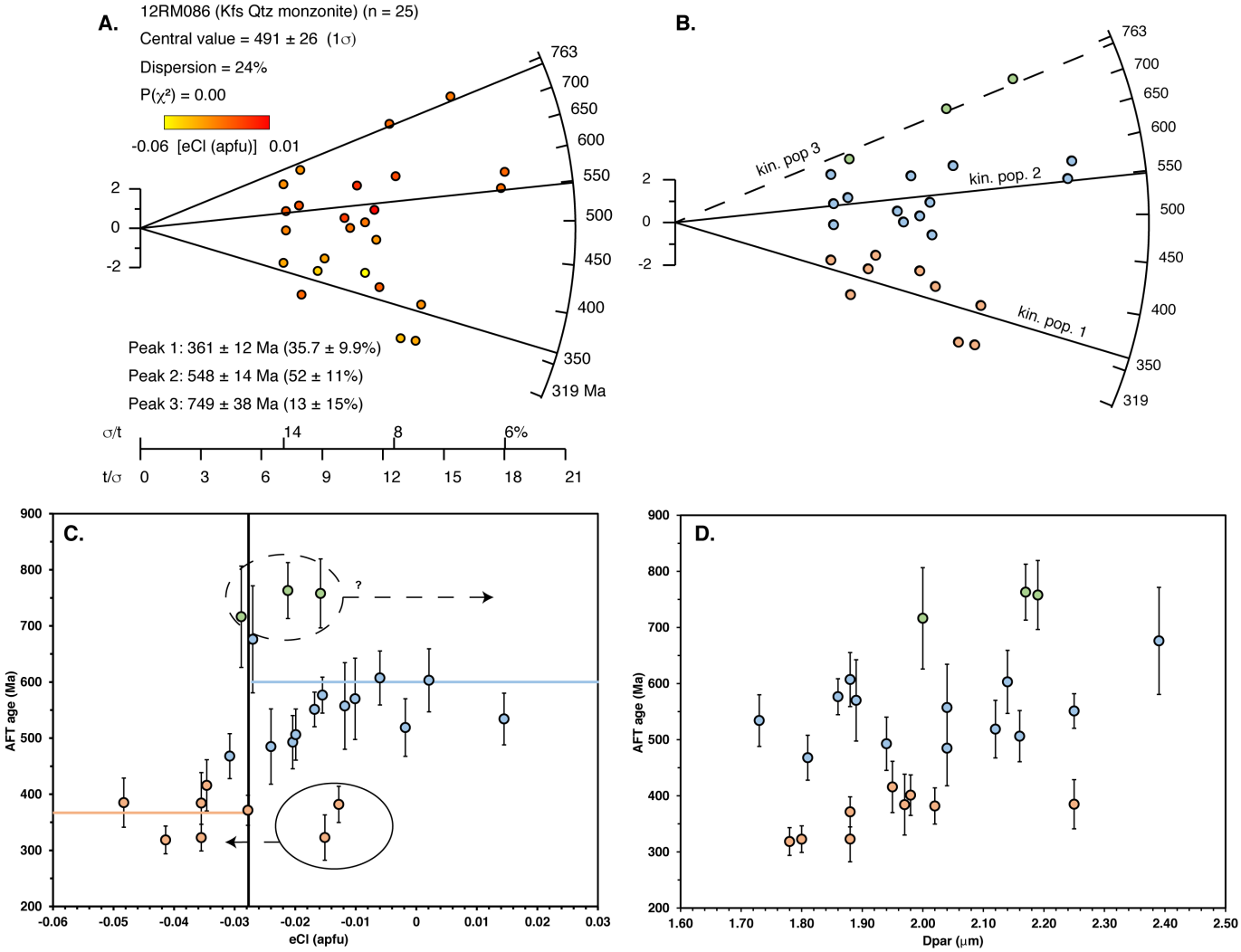

Figure 8: Plots for apatite fission-track (AFT) K-feldspar quartz (Kfs Qtz) monzonite sample 12RM086 from northern Ontario. **(A)** The radial plot for this sample shows a clear relationship between eCl (given in atom per formula unit (apfu)) and AFT single-grain age and radial-plot mixture modelling identifies three age populations. Age mixture modelling is done in DensityPlotter software v. 8.4 ([63, 64]) and results in the identified age populations, which are labelled as peaks 1, 2, and 3. **(B)** Interpreted age populations based on age and eCl are used for separating kinetic populations, which generally match distinct age peaks selected by radial-plot mixture modelling. **(C)** Age populations in eCl space. There may be a poorly resolved third age population (ca. 750 Ma) present in this sample; alternatively, the sample is a highly dispersed two-population sample (composition would favour the latter). The higher precision single-grain ages cause χ^2 failure if only two populations are chosen and include the old grains from the potential third population. Horizontal coloured bars represent the pooled ages for each population, nearly the same as the age peaks picked in panel A. **(D)** Single-grain ages with respect to D_{par}; there is a subtle relationship, but much greater overlap, between populations than on the eCl plot.

history models in this paper are in the range of approximately 0.1 to 0.7, which is considered ideal [73].

The ML model (Fig. 9A) shows a preferred maximum temperature of 54 °C with protracted burial heating lasting until approximately 200 Ma. Maximum heating (52 °C) occurs earlier at 283 Ma for the MP model T–t path. The EX model suggests maximum temperatures of approximately 70 °C at ca. 430 Ma (for the upper 95% credible interval) and approximately 40 °C for the EX path during post-depositional maximum burial heating between approximately 375 and 335 Ma. Figure 9B shows the fits to the track-length distribution and the AHe age data. The 'comparative' GOF function is used to assess the AFT central age and MTL fits, since QTQt uses a log-likelihood merit function. In Figure 9B, fits are calculated using the age- and length-fitting methods outlined in Ketcham [72], using the Kolmogorov-Smirnov (K-S) statistic for the FT lengths. The ML T–t history produced an AFT age GOF of 0.93 and MTL GOF of 0.55, and the EX T–t path yields an age GOF of 0.92 and MTL GOF of 0.50. The relationship between observed and predicted AHe ages and AFT central age (Fig. 9c) shows overall agreement between both thermochronometers, where only the oldest AHe date is misfit. There is suitable sampling of E_b (not shown) for the AHe ages, with most grains having values that range between 40 and 55 kJ/mol, suggesting that these apatites have accumulated significant alpha-recoil damage and vacancy clustering creating higher trapping power for ^{4}He diffusion [128]. These combined AFT+AHe results suggest lower maximum temperatures when compared with the HeFTy model for sample 09SZ-21-01L (AFT data only) from Pinet et al. [93], which exhibited maximum temperatures between approximately 65 and 85 °C.

6.2 *Southampton Island thermal-history model: sample 07CYA-M38B*

The explicit T–t boundary conditions imposed on the model for sample 07CYA-M38B are as follows: the maximum allowed heating/cooling rate ($\delta T/\delta t$) is 2 °C/Ma, the prior (initial) T–t space ranges from 1000 to 0 Ma and 200 to 0 °C; and the only imposed geological constraints are an Ordovician stratigraphic age of 455 ± 5 Ma at a surface temperature of 20 ± 10 °C and a modern surface temperature of 5 ± 5 °C. Sample 07CYA-M38B is modelled with only AFT data—these data exhibit multikinetic behaviour with three kinetic populations. The modelled thermal history is shown in Figure 10A. The models in Figure 10A–H are presented differently to show the posterior likelihood for the T–t path of each model; this is essentially equivalent to visualizing the derivation of the MP model T–t path without explicitly showing it. The simpler model with less constraints (MP T–t path, not shown) shows maximum heating to 88 °C at 415 Ma (surface temperature of 30 °C reached by ca. 120–115 Ma), whereas the T–t history envelope shown in Figure 10A suggests post-450 Ma heating of up to approximately 95 °C at 405 Ma, followed by monotonic cooling only until present. The EX model T–t path suggests maximum heating to 79 °C at 376 Ma and histories are coloured by the sampled posterior probability, with warmer colours being more highly probable. The observed and predicted central ages and MTL fits to individual modelled (kinetic) age populations are shown in Figure 10B–D. There are some T–t paths in the EX model that suggest cooling to surface

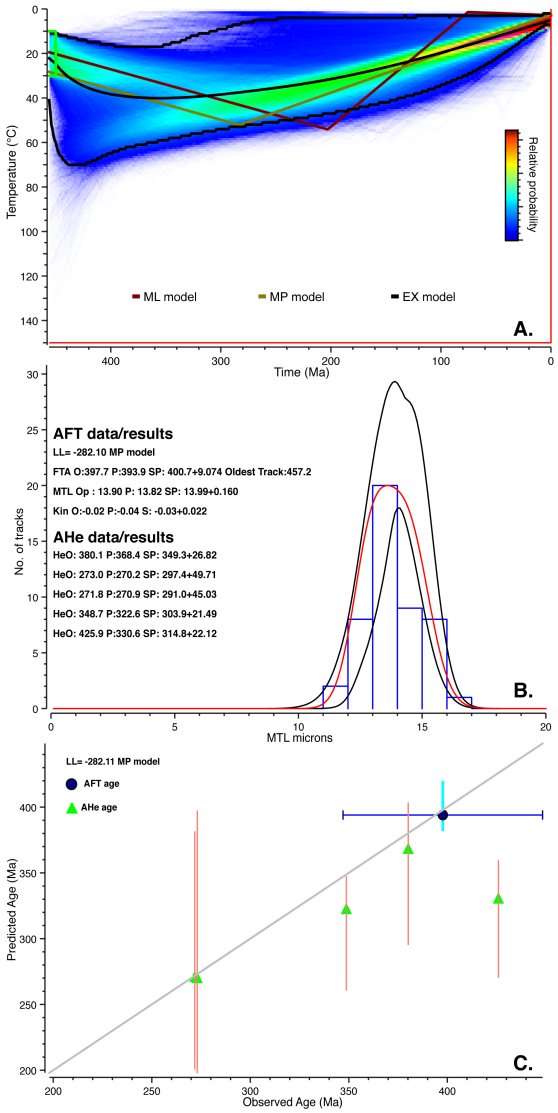

Figure 9: **(A)** Thermal-history model in QTQt (Gallagher, 2012) for apatite fission-track (AFT) and apatite He (AHe) data from sample 09SZ-21-01L from Southampton Island, Nunavut; warmer colours indicate higher relative probability. Note that only the 0 to 450 Ma part of the model is shown because the pre-depositional history is not required to explain the data and was omitted by QTQt. Black lines signify the expected (EX) model weighted-mean T–t path and model 95% credible interval. Gold line represents the maximum posterior (MP) model and is superimposed on the maximum likelihood (ML) model T–t path (i.e., the ML and MP models are the same). **(B)** Fits to AFT (log likelihood (LL)) central age (fission-track age (FTA)), mean track length (MTL), and AHe data. Individual prediction codes refer to the observed (O), predicted (P), and sampled (SP) values of the predicted value, as well as to the kinetic parameter (kin) and eCl; 'Oldest track' refers to the AFT retention age. **(C)** Observed vs. predicted ages for both AFT and AHe data, showing good agreement between observed and predicted ages. Vertical bars represent the sampled age range during the Markov chain Monte Carlo search allowed by the AFT kinetics/central age error (blue lines) and the E_b parameter for He diffusion (orange).

in the latest Triassic–early Jurassic (~20% posterior probability; Fig. 10A).

An alternate scenario is shown in Figure 10E, imposing surface conditions in the late Mesozoic. The EX model that allows Cretaceous and younger reheating is shown in Figure 10E. The explicit boundary conditions imposed on the alternate model are as follows: the maximum allowed heating/cooling rate (δT/δt) is 2 °C/Ma; the prior (initial) T–t space ranges from 900 to 0 Ma and 180 to 0 °C; and the imposed history constraints are a broad high-temperature constraint of 150 ± 30 °C at 800 ± 100 Ma (to allow cooling and setting of older third AFT-age population), a near-surface temperature constraint of 20 ± 10 °C at 455 ± 5 Ma as well as another constraint of 20 ± 10 °C at 110 ± 10 Ma (kimberlite xenoliths and regional unconformity), and a modern surface temperature of 5 ± 5 °C. The geological justification for an alternate model with cooling to the surface in the Mesozoic comes from the regional Cretaceous unconformity, which suggests uplift and erosion occurred before widespread Albian deposition and the emplacement at ca. 65–85 Ma of the Nanuq kimberlites some 175 to 200 km to the west; these contain nonmarine mudclast xenoliths that host mid-Albian to early Cenomanian palynomorphs [129]. In this model, post-450 Ma heating of mean 78 °C occurs at ca. 365–360 Ma (~62–84 °C at 95% CI) for the EX T–t path and greater maximum heating allowed at ca. 398 Ma to approximately 44–89 °C, when considering the full 95% CI envelope). Cooling ensues after 360 Ma until sometime between 170 and 112 Ma, when rocks are at surface temperatures of approximately 30 °C. Minor reheating occurs until a thermal peak of 48 °C (upper 95% limit) is reached at ca. 77 Ma. The MP model shows a thermal maximum at 420 Ma (85 °C), which is apparent from the red (90–100%) posterior paths in the EX model (Fig. 10E). This sample was tentatively modelled as three populations, but the model results for sample 07CYA-M133 are considered more reliable.

6.3 Southampton Island thermal-history model: sample 07CYA-M133

Sample 07CYA-M133 is modelled with AFT data only (Fig. 11A–F), therefore the data are somewhat limited in terms of what can be surmised about the Mesozoic through Cenozoic history below 70 °C. The explicit boundary conditions imposed on the model for 07CYA-M133 are as follows: the maximum allowed heating/cooling rate (δT/δt) is 5 °C/Ma for initial runs and reduced to 2 °C/Ma for the final run shown here (Fig. 11A); the prior (initial) T–t space ranges from 800 to 0 Ma and 150 to 0 °C; and the only imposed history constraint is a near-surface temperature of 20 ± 10 °C at 455 ± 5 Ma and modern surface temperature of 5 ± 5 °C. The T–t space was made smaller for this model because the larger prior was unnecessary in this case, and in early trial models the histories generated were simpler due to the Bayesian penalty on complexity. The modelled thermal history shows a minor and temporally broad post-450 Ma heating event with maximum temperatures being 67 °C and 48 °C for the ML and MP models, respectively. The EX weighted mean T–t path suggests slow heating up to 55 °C until approximately 205 Ma (upper 95% credible interval of ~70 °C). Noticeably, the ML and MP models suggest either a double heating pulse history or extended heating until ca. 100 Ma, followed by cooling, respectively. These scenarios would both necessitate latest Mesozoic to early Cenozoic heating.

The fits to the AFT central age and the track-length distribution can be used to generally determine how applicable the various model T–t paths are with respect to the observed data. It should be reiterated that the GOF values shown for QTQt are a crude measure of the respective statistical fit to the observed data and are presented only for comparison. The ML-model GOF is 0.13 for central age and 0.95 for track length, whereas GOF values are of 0.26 for age and 0.81 for length for the MP model, and 0.84 for age and 0.10 for length for the EX model. The GOF is generally poor (<0.3) for either the central age (ML and MP models) or length (EX model), which suggests that the thermal history is poorly constrained under the imposed model assumptions. An alternate model is shown (Fig. 11D) that incorporates the Cretaceous surface constraint at 110 ± 10 Ma, which was also tested to compare AFT data fits with the simpler first model (Fig. 11A). The fits for each T–t paths in the alternate model are as follows: the ML model GOF is 0.17 for central age and 0.90 for length, the MP model GOF is 0.18 for age and 0.09 for length, and the EX model GOF is 0.96 for age and 0.00 for length. The GOF is poor for the age (ML), the length (EX), or both (MP). The best fits to the track lengths occur in models where there is a late reheating (i.e., the ML T–t path in the first model and the ML T–t path in the alternate model), which suggests greater or longer heating is required to adequately fit the lengths, and, in both models, the resulting ML T–t paths are nearly identical regardless of imposed geological constraints, suggesting a late reheating event provides a better fit to the AFT data in either case; however, overall the AFT data are poorly fit without imposed constraints in QTQt.

The different QTQt models suggest that two thermal pulses better explain the AFT data. However, considering the lack of satisfactory T–t resolution encountered during QTQt modelling, this sample was investigated further using the AFTINV software to further explore geologic assumptions (Fig. 12A–F). The explicit boundary conditions of this sample were applied to the model as in QTQt, but in this case random MC and the CRS algorithm were used to investigate a Cretaceous burial scenario. Exploratory random heating/cooling history models suggest two thermal events provide a better fit to the AFT data. The track-length distribution for sample 07CYA-M133 is characterized by a broad peak that is difficult to fit with a single heating pulse. Heating either had to be over a prolonged period, which is less reasonable given the long timescale (and the regional geology), or, more likely, a second heating event occurred in the late Mesozoic. In this case, the goodness-of-fit was calculated using the lowest maximum objective function in AFTINV (same method as HeFTy; the minimum combined objective-function GOFs are also reported) because the modelled track lengths are a better match to the observed lengths and produce a more reasonable, 'smooth' T–t history.

The explicit AFTINV boundary conditions applied during modelling are as follows: the maximum allowed heating/cooling rate (δT/δt) is 2 °C/Ma; the initial T–t space ranges from 800 to 0 Ma and 150 to 0 °C; and a minimum temperature of 15 °C is applied to the entire model and a present-day maximum surface temperature of 10 to 15 °C is allowed. There are 81 total model time steps at 10 Myr each and the thermal histories are required to start between 130 and 150 °C at the first 800 to 790 Ma time step. The model can search for two random heating events within the initial T–t space. The first thermal minimum can be

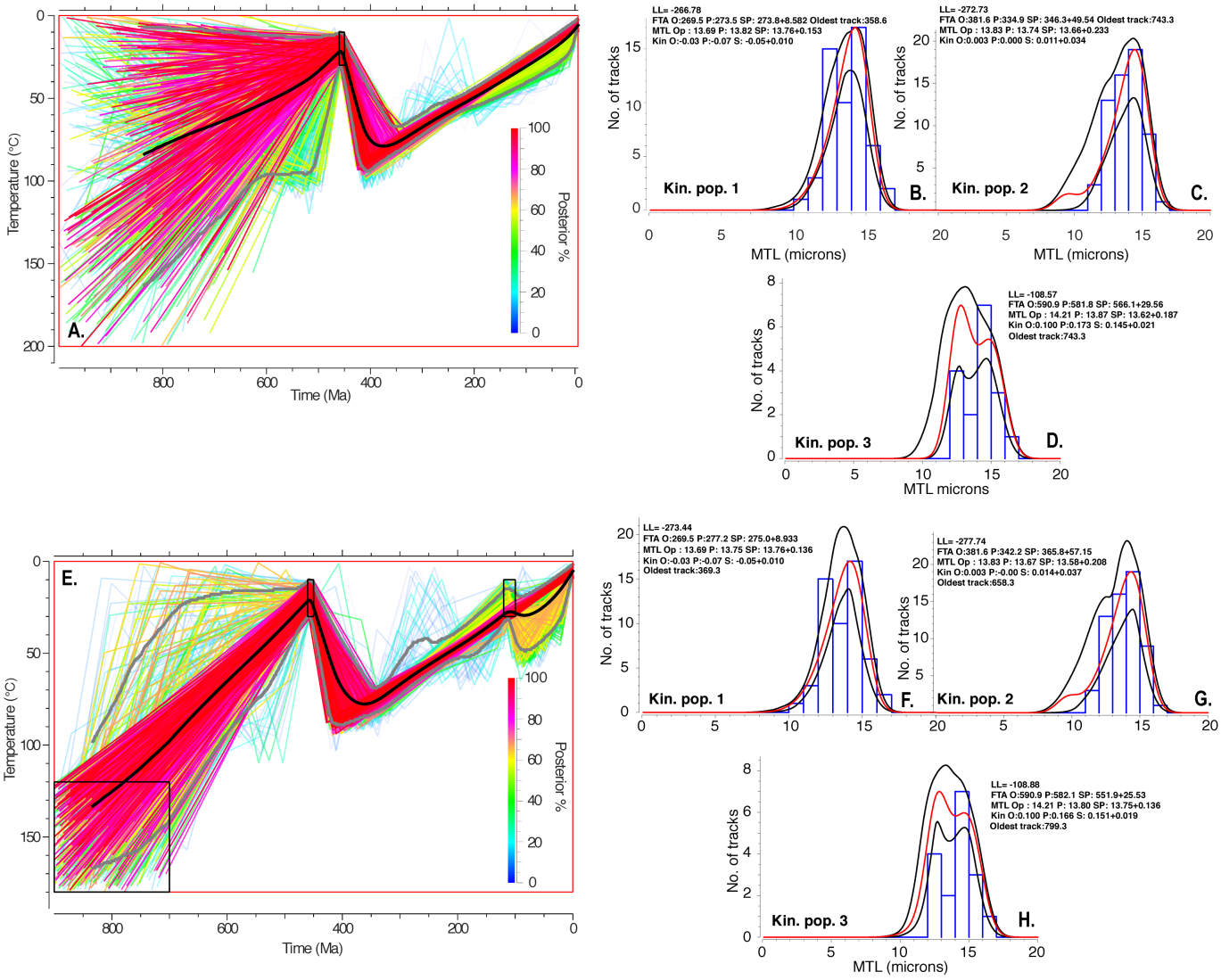

Figure 10: **(A)** Expected (EX) thermal-history model in QTQt for sample 07CYA-M38B from Southampton Island, Nunavut, with Ordovician geological constraint (black bordered box) only; warmer colours indicate higher posterior probability, and black lines signify the EX model weighted-mean T-t path and model 95% credible interval (grey line). **(B–D)** Fits to apatite fission-track (AFT; (log likelihood (LL)) central age (fission-track age (FTA)) and mean track length (MTL) for each kinetic population (Kin. pop.). **(E)** Alternate, preferred QTQt EX model, with additional geological constraints (black bordered boxes) imposed. **(F–H)** Fits to AFT central age and MTL for each kinetic population. Individual prediction codes refer to observed (O), predicted (P), and sampled (SP) values of the predicted value, as well as to the kinetic parameter (kin); 'Oldest track' refers to the AFT retention age. Red box represents the 'prior' T–t space searched.

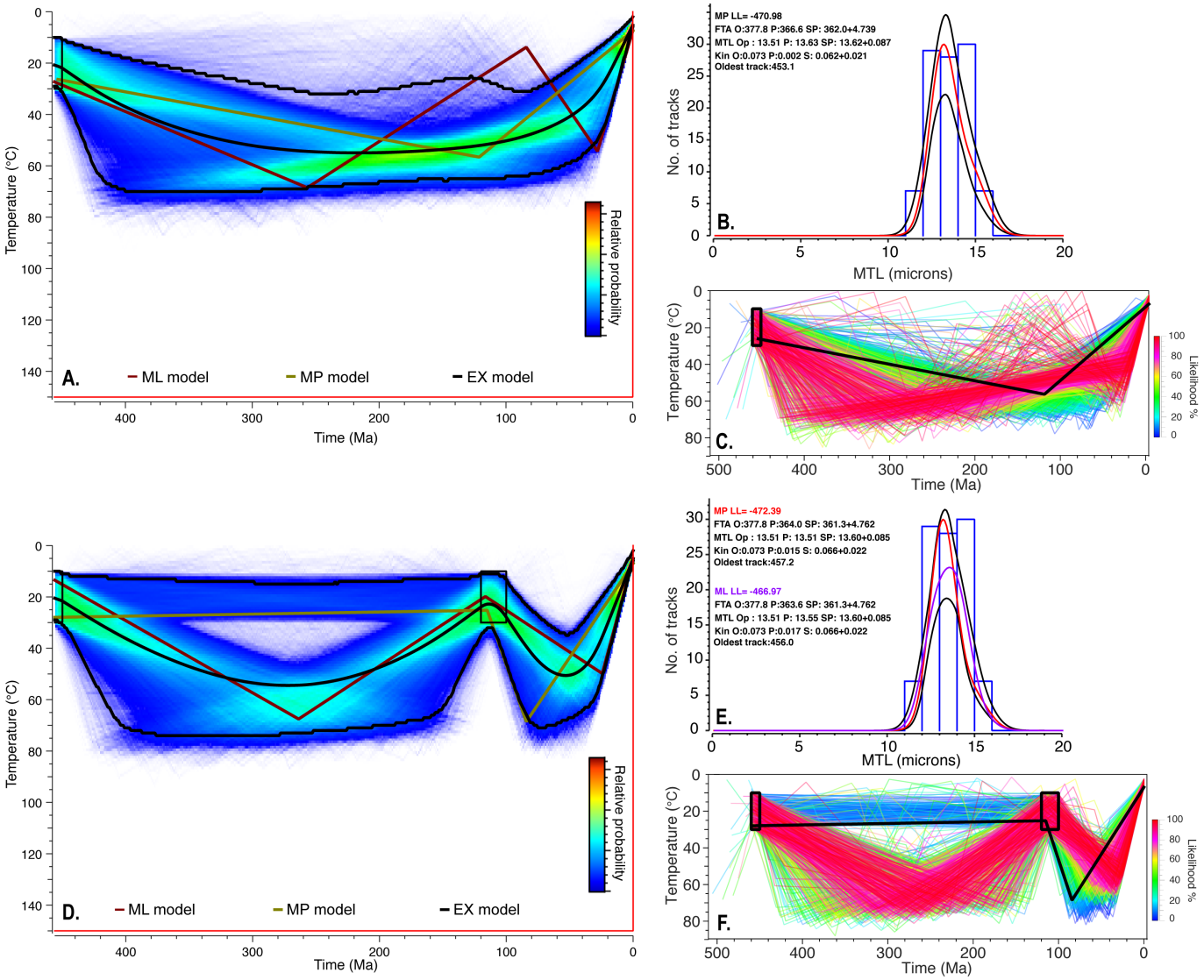

Figure 11: **(A)** Expected (EX) thermal-history model in QTQt for sample 07CYA-M133 from Southampton Island, Nunavut, with Ordovician geological constraint only; warmer colours indicate higher relative probability. Note that only the 0 to 460 Ma part of the model is shown because the pre-depositional history is not required to explain the data. Black lines signify the EX weighted-mean T-t path and model 95% credible interval. **(B)** Fits to apatite fission-track (AFT) central age and mean track length (MTL) for the maximum posterior (MP) model T-t history. **(C)** The MP model T-t history (black line) with all individual solutions coloured by likelihood (warmer = greater likelihood). **(D)** Alternate model, with imposed Cretaceous surface constraint, coloured by relative probability, same as in panel A. **(E)** Fits to AFT central age and MTL for the MP and maximum likelihood (ML) T-t histories. **F)** The MP model T-t history (black line) with all individual solutions coloured by likelihood (warmer = greater likelihood). Individual prediction codes refer to observed (O), predicted (P), and sampled (SP) values of the predicted value, as well as to the kinetic parameter (kin); 'Oldest track' refers to the AFT retention age. Black boxes in panels A, C, D, and F are geological constraints discussed in the text.

between 500 and 450 Ma (Ordovician deposition), whereas the second thermal minimum is broadly searched for between 300 and 100 Ma. The model was run until 300 solutions were found at the 0.05 level that fit the observed AFT pooled ages and c-axis projected track lengths for the single kinetic population. This model pool was then retained for the CRS algorithm to improve the 0.05 solution set to the 0.5 level.

Figure 12 shows the AFTINV modelling results for sample 07CYA-M133 at the 0.05 level (Fig. 12A) and at the 0.5 level (Fig. 12B) after the CRS algorithm refined the initial 300 random MC 0.05 solutions (light grey paths). Note that three solutions randomly found in the 0.05 solution set passed at the 0.5 significance level (dark grey paths). All 300 solutions were improved to the 0.5 confidence level (dark grey paths in Fig. 12B). Only the CRS 0.5 level-model solution will be discussed in detail, as it provides a better overall fit to the AFT data. Figure 12C shows the 'measured' eCl range, assigned eCl value for the population, and the 0.5 significance-level model fits to the observed AFT data. The modelled thermal histories provide excellent fits (GOF = 0.83) to the AFT lengths and moderate fits to age (GOF = 0.15) because of the higher retentivity r_{mr0} value used during modelling and the use of the lowest maximum objective function for fitting (for comparison the lowest combined minimum objective-function GOFs are 0.89 for AFT age and 0.77 for the lengths). In Figure 12D–F, the timing and magnitude of heating during both thermal peaks are shown.

Whether the Precambrian bedrock was fully exhumed prior to the Ordovician remains uncertain, therefore a maximum temperature of 40 °C is allowed for the first thermal minimum where the 'depositional age' (DA) or timing of basement exposure is 480 Ma for the minimum objective-function solution, which is just prior to Ordovician carbonate deposition in the Southampton Island area. However, the mean DA for all 300 solutions is 468 ± 14 Ma and encompasses the Ordovician depositional age (Fig. 12A, B). The first thermal maximum occurs at temperatures between 88 °C and 102 °C (93 ± 3 °C average), ranging from 330 to 440 Ma (373 ± 20 Ma average), whereas the second thermal peak is between 68 °C and 80 °C (73 ± 2 °C average) occurring at 63 ± 17 Ma. The compositional range for sample 07CYA-M133 apatite is very broad with respect to the other FT samples and, therefore, kinetic adjustment within this range would modestly affect the achieved maximum temperature. The predicted Ro values range from 0.55 to 0.57% at the 0.5 level (0.54–0.62% at 0.05 level), which agrees with the %Ro-equivalent values from Southampton Island Ordovician shale units [103]. To clarify the AFT–Ro maximum temperature agreement, the modern, calibrated BasinRo% vitrinite-reflectance model of Nielsen et al. [130] was used rather than the Sweeney and Burnham [131] EASY%Ro model because the latter begins to overpredict the temperature–Ro relationship at values greater than 0.5% (i.e., Ro values are too high for a given temperature up to ~1.75% Ro).

Though the 07CYA-M133 results from the two different software packages do not completely agree, they are actually quite comparable in terms of temperature. They differ in thermal-history style due to fundamental assumptions about the history and the difference in the utilized statistical/T–t search approach. The QTQt-generated model suggests that two thermal peaks are more likely to explain the AFT data, and this scenario was explicitly enforced in AFTINV. The QTQt model results illustrate that the data are not easily explained by a simple history over that long timescale and are effectively demonstrating this with multimodal solutions. Likewise, the AFTINV results suggest that cooling to the near surface occurred before the Cretaceous, during Carboniferous through Jurassic time, agreeing with Ault et al. [94] thermal-history models for the Slave Craton and implying the early–mid Mesozoic was probably a time of regional erosion.

6.4 *Northern Ontario thermal history model: Precambrian sample 12RM086*

The thermal-history model results for sample 12RM086 were presented in Pinet et al. [132] and were generated using the AFTINV software. In the initial model from this paper, modelling of the AFT data was based on the assumption that discrete thermal events occurred in the Paleozoic and late Mesozoic, consistent with preserved strata in the nearby Hudson Bay and Moose River basins. Potassium-feldspar from a sample in the North Caribou terrane in northern Ontario was analyzed by the $^{40}Ar/^{39}Ar$ step-heating method [8] and interpreted using the multidiffusion domain (MDD) model [133, 134, 135]; the resulting data indicated the rocks were subjected to temperatures ranging between 150 and 200 °C during the Tonian (1000–850 Ma). The $^{40}Ar/^{39}Ar$ MDD sample was collected approximately 250 km west of sample 12RM086 and, therefore, this relatively high-temperature constraint was applied to the latter during modelling. The paleodepth of sample 12RM086 during the early phase of regional deposition of Paleozoic sediments (Late Ordovician, ca. 450 Ma) is unknown, but can be tentatively estimated to be less than 1.7 km (or < 50 °C) by using a maximal slope toward the basin centre of 2 °, typical of the Hudson Bay Basin and most intracratonic basins worldwide [136].

The explicit AFTINV boundary conditions applied during modelling are as follows: the maximum allowed heating/cooling rate ($\delta T/\delta t$) is 2 °C/Ma; the initial T–t space ranges between 900 to 0 Ma and 200 to 0 °C; and a minimum temperature of 15 °C is applied to the entire model and a modern surface temperature of 15 to 20 °C is allowed. There are 171 total model time steps of 5 Myr each and the thermal histories are required to start between 200 and 150 °C at the first 900 to 895 Ma time step. The model is allowed to search for two random heating events within the initial T–t space, which are required to be between 30 and 150 °C for the first thermal peak, and 20 and 150 °C for the second peak. The first thermal minimum is allowed to be between 750 and 450 Ma (timing of Ordovician deposition), whereas the second thermal minimum is searched for between 180 and 115 Ma (period of Attawapiskat/Victor kimberlite emplacement and Mesozoic deposition in the Moose River Basin). The model was run until 300 solutions were found that fit the observed AFT pooled ages and *c* axis projected track lengths for both kinetic populations at the 0.05 significance level. This model pool was then retained for the CRS algorithm to improve the 0.05 solutions to the 0.5 level, where 300 solutions were also found.

Figure 13A–G shows the AFTINV modelling results for sample 12RM086 at the 0.05 level (Fig. 13A) and at the 0.5 level (Fig. 13B) after the CRS algorithm refined the initial 300 random MC 0.05 solutions (light grey paths). Note that eight solutions found

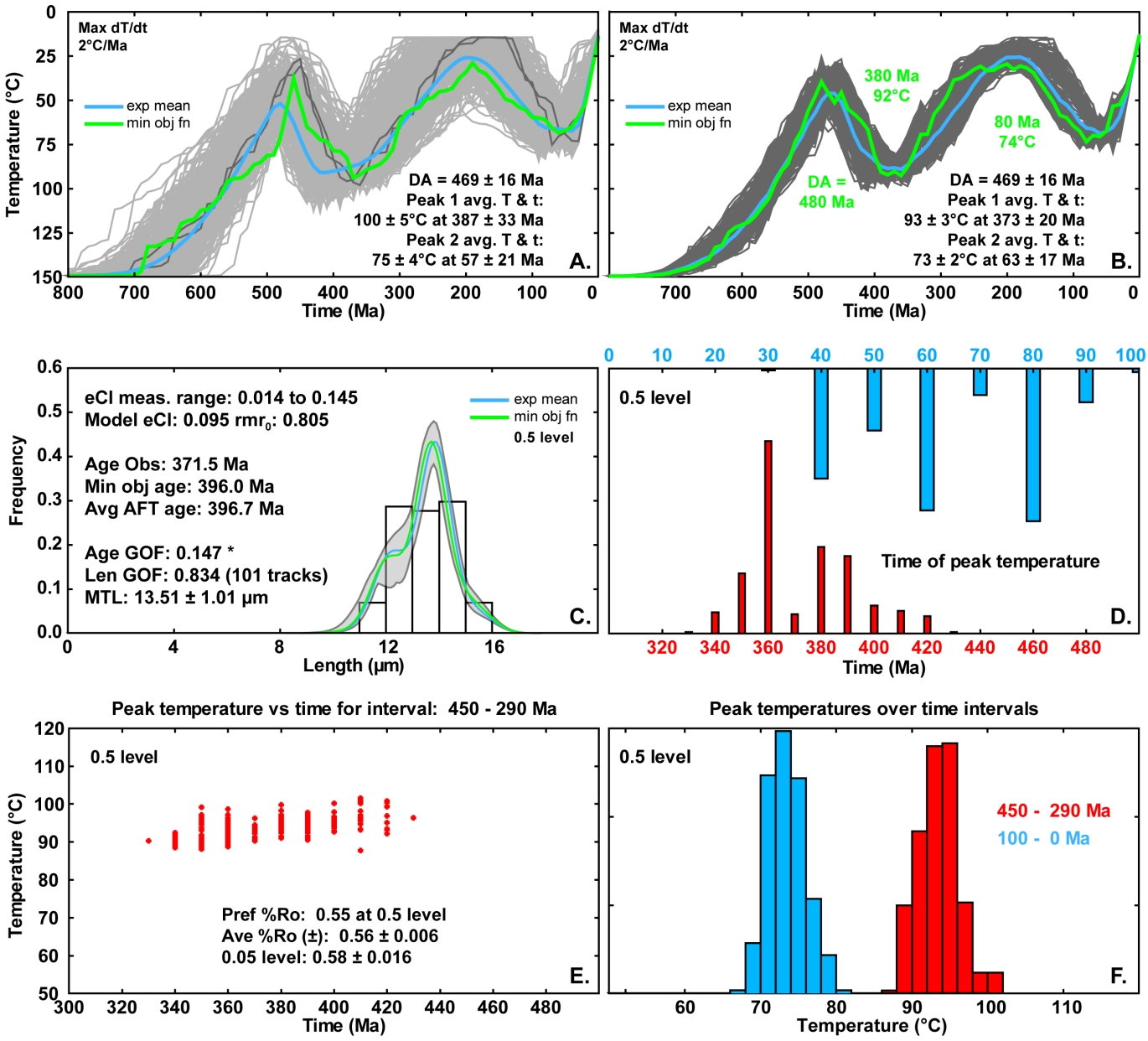

Figure 12: Thermal-history model in AFTINV for sample 07CYA-M133 from Southampton Island, Nunavut. **(A)** Three hundred acceptable random Monte Carlo (MC) solutions at the 0.05 significance level (light grey T-t paths). Note: dark grey paths in the 0.05 envelope are those that happened to pass at the 0.5 level during the initial MC search. The exponential mean (exp mean) solution (blue line) and the best-fit minimum objective-function (min obj fn) solution (green line) are also shown. **(B)** Three hundred acceptable solutions at the 0.5 significance level (dark grey T-t paths) obtained using the controlled random-search algorithm. **(C)** Fits to the observed (obs) apatite fission-track (AFT) age and mean track length (MTL) data for kinetic population no. 1. Note the age goodness-of-fit (GOF) is lower in this case because 1) the length (len) fit is emphasized by the use of the lowest maximum objective function and 2) a more retentive rmr0 kinetic value (i.e., greater than the average value but within the measured eCl range) is applied in the model. The calculated (meas.) eCl range is given along with the assigned value used during modelling. **(D)** Timing of peak temperatures for the 500 to 290 Ma and 100 to 0 Ma intervals. **(E)** Peak temperatures for the time interval 500 to 290 Ma. **(F)** Peak-temperature histograms at the 0.5 level for each time interval. DA = 'depositional age'; Pref %Ro = best fit %Ro; Ave %Ro = average %Ro and standard deviation.

in the 0.05 set passed at the 0.5 significance level (dark grey paths). All 300 solutions were improved to the 0.5 confidence level (dark grey paths in Fig. 13B). Only the CRS 0.5 level-model solutions are discussed in detail, as these paths provide a better overall fit to the AFT data. Figure 13C, d shows the 'measured' calculated eCl range, assigned eCl value for each population, and the 0.5 confidence level model fits to the observed AFT data. The modelled thermal histories provide excellent fits (GOF ~90–99%) to both AFT age and length distribution.

The AFTINV model was set up to allow an initial, randomly selected "depositional age" thermal minimum followed by two random heating events. In the present case, this is a pseudo-depositional age, or the time at which the sample presumably cooled upon exhumation to the surface, and occurs at 548 ± 21 Ma (average of 300 solutions at the 0.5 confidence level). The first thermal peak occurs between 355 and 445 Ma (400 ± 26 Ma average) and reaches an average temperature of 72 to 80 °C (75 °C average; Fig. 13E–F), whereas the 0.05 confidence-level solutions suggest that peak heating up to 89 °C during the Paleozoic cannot be ruled out by the model. The second thermal peak is at 76 ± 15 Ma at the 0.5 level and reaches average temperatures between 47 and 61 °C (55 °C average). The later thermal maximum can be thought of as the highest temperature allowed by the AFT data before further resetting occurs. The best-fit T–t path at the 0.5 confidence level predicts a depositional age of 535 Ma, maximum temperature of 76 °C at 380 Ma, and a maximum temperature of 56 °C during later heating at 95 Ma. This thermal history demonstrates that two distinct thermal peaks sufficiently explain the AFT data under the assumption that bedrock exhumation to surface occurred in the latest Neoproterozoic to early Cambrian. The predicted %Ro reflectance values for the thermal-history solutions (< 455 Ma) at the 0.5 confidence level range from 0.48 to 0.49% and are in good agreement with regional thermal maturity data for the Hudson Bay region [95, 103], and with %Ro data generated for the Boas River shale in northern Ontario [137].

7 MODELLING INTERPRETATIONS AND CONCLUSIONS

During modelling, application of tight regional T–t constraints was avoided and only done so in some instances to test the plausibility of different scenarios. This was done to reduce user modelling bias and investigate the T–t resolving power of the thermochronology data. First, the modelling results for Southampton Island are summarized. The primary burial phase began during the Ordovician, in agreement with preserved strata in Hudson Bay and Southampton Island. Burial heating continued through the Devonian, when maximum burial was achieved. The differences in maximum Paleozoic (burial) temperatures can potentially be explained by the position occupied by the sample relative to the normal fault array that bounds Southampton Island to the north, or by differences in apatite chemistry, and therefore retentivity. The sample that yielded the higher maximum paleotemperature (07CYA-M133) was also collected closest to the fault array, suggesting broad footwall uplift adjacent to large, steep, normal faults. The sample that yielded the lower maximum paleotemperature (09SZ-21-01L) is from Ordovician sandstone (stratigraphically higher position) and was located the farthest from the fault array. Notably, sample 07CYA-M133 contained a broad range of apatite compositions, which allowed for a range of peak temperature sensitivity depending on the representative r_{mr0} value chosen for modelling. The modelled maximum paleotemperature for sample 09SZ-21-01L agreed well with results from Rock-Eval 6 analyses, reflectance petrography, and preliminary clumped-isotope analyses for replacement cements, and indicated that higher paleotemperatures, suggested by fluid inclusions, were not regionally representative. Cooling and erosion occurred in the Permian to Triassic and near-surface temperatures were reached (< 30 °C) by about 140 Ma, based on the MP/ML models for sample 09SZ-21-01L. In addition, a relatively good-fit temperature history for sample 07CYA-M133 was found only in the case where the sample had been exhumed to the surface by the late Mesozoic and subsequently buried.

The lack of regional early–mid Mesozoic sediments in this area lends some confidence to the notion of erosional denudation being the dominant process until the Cretaceous. This scenario gains support from sparse Mesozoic sedimentary constraints in southern Hudson Bay [108], undated (presumed late Mesozoic) half-graben infill in Hudson Strait [101, 102], and xenoliths found in kimberlites. Additional near-surface constraints can be tentatively inferred from the nearby Rankin Inlet kimberlites, which are approximately 200 km west of Southampton Island and range in age from ca. 225 to 170 Ma, with the majority emplaced between 204 and 181 Ma [138]. These kimberlites do not contain overburden xenoliths of Paleozoic–Mesozoic age. The kimberlites may have been emplaced into Precambrian basement without Phanerozoic cover, because other locations across the Slave and eastern Rae-Churchill cratons that were buried in the Phanerozoic usually contain xenoliths of cover strata [139, 123, 140, 129, 141], or were emplaced into Phanerozoic strata that has remained preserved [e.g., 122].

The EX T–t model of sample 09SZ-21-01L from Southampton Island suggested rocks were never deeply buried there subsequent to the Ordovician, with perhaps only a maximum of about 1.0 to 2.2 km of post-Ordovician cover, assuming a 15 °C surface temperature and conservative 25 °C/km geothermal gradient. There are approximately 500 m of preserved strata on Southampton Island [95], suggesting that approximately 0.5 to 1.7 km of rocks were eroded since the late Paleozoic, with most eroded strata probably being Devonian clastic-wedge sediments [142]. The ML model T–t path also suggests that the sandstone sample was exhumed to the surface by Cretaceous time.

Significant Cretaceous burial during the Cretaceous on Southampton Island is unlikely. Sample 09SZ-21-01L was at the surface in the Ordovician and buried in the Devonian, thus partially resetting the AHe dates and suggesting cooling in the latest Paleozoic–early Mesozoic. Strata approximately 2.6 km thick in the offshore Hudson Strait are tentatively assigned a Cretaceous age [109, 116] and suggest faulting was active in the late Mesozoic, with deposition in half-grabens occurring during regional tectonic adjustment and failed rift opening of the Hudson Strait [102]. The paleo-Bell River system was also a potential source for minor, localized clastic sediment input during latest Cretaceous–Tertiary fluvial drainage of Western Canada through the Hudson Strait to the Atlantic Ocean [143, 144]. The data and models presented here provide mixed results in support of Cretaceous burial of Southampton Island during the purported Albian seaway, but do not rule out deposition of 3 km or less

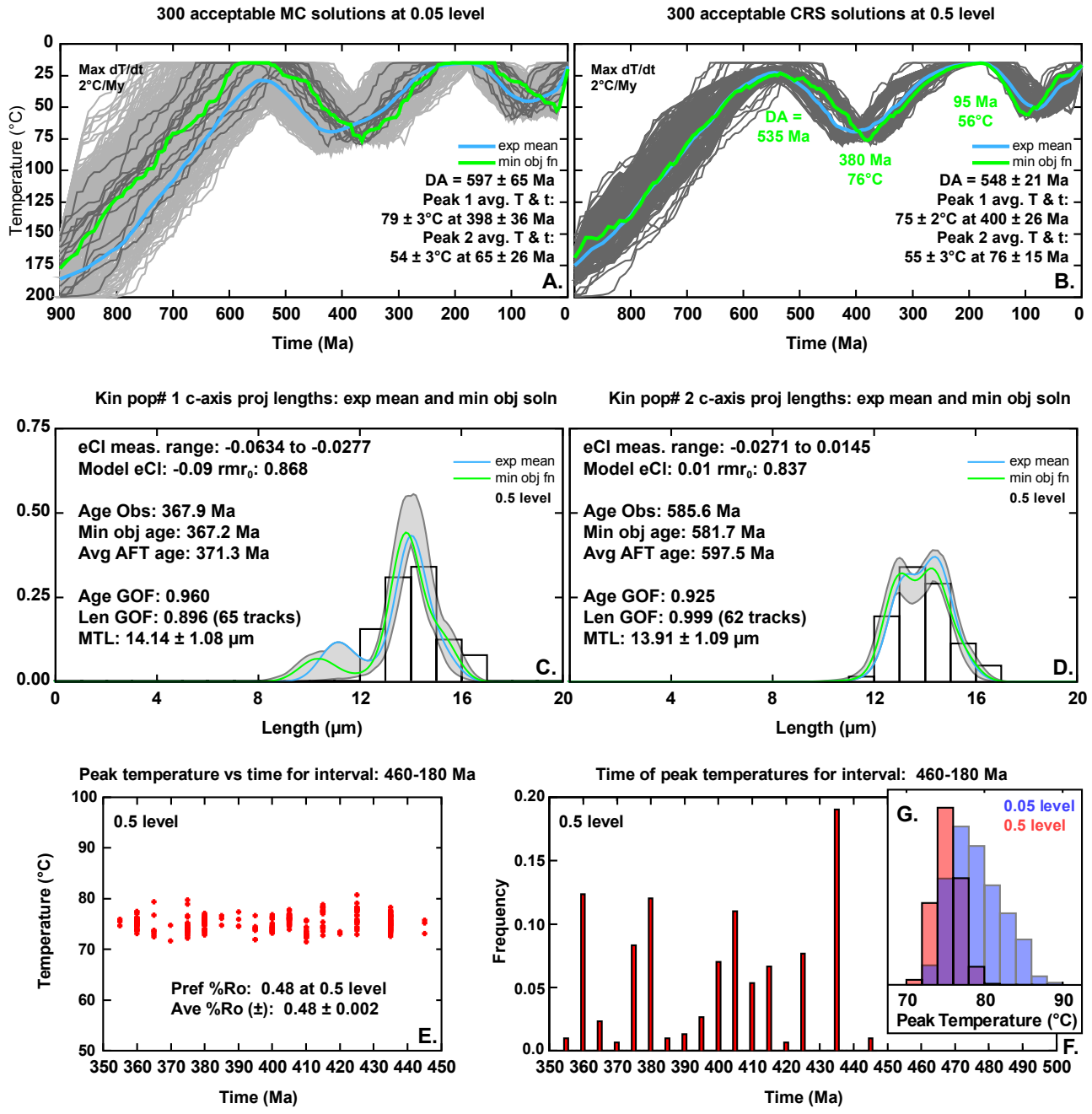

Figure 13: Thermal-history model in AFTINV for sample 12RM086 from northern Ontario. **(A)** Three hundred acceptable random Monte Carlo solutions at the 0.05 significance level (light grey T-t paths). The exponential mean (exp mean) solution (blue line) and the best-fit minimum objective-function (min obj fn) solution (lowest combined objective function; green line) are also shown. Note that some 0.5 solutions were randomly found during the initial MC search (dark gray paths). **(B)** Three hundred acceptable solutions at the 0.5 significance level (dark grey T-t paths) obtained using the controlled random-search algorithm. **(C)** Fits to the observed (obs) apatite fission-track (AFT) age and mean track length (MTL; len) data for kinetic population no. 1. **(D)** Fits to the observed AFT age and length data for kinetic population no. 2. In both panels C and D, the calculated (meas.) eCl range is shown along with the assigned value used during modelling. **(E)** Peak temperatures for the time interval 500 to 170 Ma (the time axis is truncated because no values occurred outside the range shown). **(F)** Timing of peak temperatures for the first thermal peak (time axis truncated as in panel E). **(G)** Peak-temperature histograms for both the 0.05 and 0.5 level solutions over the same time interval as in panel F. GOF = goodness of fit; Pref %Ro = best fit %Ro; Ave %Ro = average %Ro and standard deviation.

during this time. A thermal history involving some localized Cretaceous burial is the preferred hypothesis based on the regional geological information and the better-fitting modelling results in favour of post-Paleozoic reheating.

The thermal history of the northern Ontario sample suggests exhumation of the Canadian Shield occurred during protracted Rodinia breakup and is consistent with peneplanation of the southern Hudson Bay region before the Cambrian. This timing is in excellent agreement with the assumed late Precambrian erosion of the Canadian Shield based on regional unconformities prior to the initiation of subsidence in North American interior basins [114, 145]. The primary thermal maximum (Fig. 13A, B) occurred during the Devonian, in agreement with the youngest preserved Hudson Bay sediments This also agrees with the sedimentary mass-balance calculations of Patchett et al. [142]; they estimated burial amounts of 0 to 2 km for distal Caledonian–Franklinian foreland deposits. The thermal-history model developed here helps provide more rigorous estimates of burial magnitude. Using the average thermal maximum of 75 °C at the 0.5 confidence level, the total amount of estimated burial is about 2.4 to 4.0 km for northern Ontario (geothermal gradients of 15–25 °C/km). Patchett et al. [142] set the hypothetical southern limit of the Devonian clastic units to offshore Hudson Bay ([142]; Fig. 2 and Fig. 4), whereas the work presented here would suggest it extends further south. Interestingly, thermal histories at the 0.05 confidence level cannot rule out deposition occurring into the late Pennsylvanian (300 Ma), as suggested by Tillement et al. [115]. Thin Cretaceous burial is highly probable in this location given the proximity to the late Mesozoic rocks in the Moose River Basin, the high sea level during the existence of the Western Interior Seaway, and the general requirement for late heating (i.e., double heating-pulse thermal history) and track-length shortening during preliminary AFT T–t modelling. Cretaceous burial was on the order of approximately 1.6 to 2.6 km (~55 °C) and likely occurred from the mid-Albian (earliest time of thermal maximum) to the Selandian (Paleocene). Conservative burial estimates at the middle-to-lower end of this range are preferred because the AFT data have uncertain sensitivity to thermal maxima at that time without accompanying AHe data.

In summary, this work offers preliminary results that are consistent with regional geology, suggesting the Hudson Bay region was buried by sediments in the Ordovician through Devonian, and later in the mid-Cretaceous. The Hudson Bay Basin succession is a preservational remnant that was more extensive and thicker than preserved rocks would suggest, based on unconformities at the basin margins and the thermochronology data presented here. The Paleozoic section in the James Bay lowlands probably extended further to the west and the best-fitting thermal histories suggest maximum burial occurred during the Early Devonian (Emsian) to Late Devonian (Famennian), seamlessly agreeing with preserved stratigraphy; however, burial continuing into the Pennsylvanian cannot be completely ruled out.

The AFT thermal-history models in this study demonstrate that the hydrocarbon-generation potential in the Hudson Bay region is moderate-to-high, yet source rocks are generally thermally immature and were never deeply buried (see Lavoie et al., this volume). The results imply long-term petroleum-system integrity is questionable and presents high exploration risk. This work has demonstrated low-temperature thermochronology can be successfully applied to determine whether areas of the Canadian Shield were blanketed in sedimentary cover throughout the Phanerozoic.

8 COMMENTS ON MODELLING STRATEGIES

The relatively fragmented sedimentary record of cratons and their inherently protracted histories pose challenges to understanding the evolution of continental interiors over long time scales using low-temperature thermochronology. Some of the ways to assist in elucidating deep-time histories include (1) using varied modelling approaches (i.e., different software and statistical methods), (2) employing multiple thermochronometer data to provide better T–t resolution [e.g., 16], and (3) adopting careful sampling strategies, such as sampling close to unconformities, which provide additional geological constraints.

One of the strengths of using software like QTQt is that the input data are used to make inferences about the complexity of the thermal history without the user making *a priori* assumptions. A 'learning' algorithm like rjMCMC provides flexibility and at the same time reduces ambiguity that is intrinsic to purely random thermal-history generation that can impede statistical-fit optimization and potentially produce longer model run times. The ability to utilize Bayesian resampling of chronometer age data and kinetic parameters also enables the modeller to include known uncertainties in kinetic models that have been extrapolated from the laboratory to the geological time scale. The added advantage of using QTQt and resampling unknown parameters is that a thermal history will be generated (often regardless of good/bad statistical fit), but the user can then examine the histories and data fits to determine where the model is fitting poorly and/or what variables may be incompatible with acceptable history generation. This latter point is important to consider for the novice user and care should be taken to fully explore many different model scenarios. A potential drawback, especially for long-term histories, is that a simpler history may be inferred incorrectly because the data do not provide enough information to justify additional complexity, which advocates for multi-chronometer data for deep-time histories [18]. This was potentially the case for sample 07CYA-M133.

Random Monte Carlo thermal-history modelling provides the user with greater control and the ability to enforce explicit boundary conditions that must be adhered to during thermal-history generation. This approach has limitations as well, because the user can make geological assumptions that may or may not be valid, there is the potential for loss of model-exploration flexibility, and there is the inability to handle large or precise data sets resulting in no acceptable thermal histories being generated (due in part to adherence to statistical p values). Vermeesch and Tian [67] and Gallagher and Ketcham [146] provided a thorough discussion on modelling strategies, statistical theory and best practices, and the strengths and weaknesses of commonly used thermochronology modelling software.

One noteworthy outcome of the modelling exercises in this work is that the predicted QTQt eCl kinetic value for each (kinetic) population follows a pattern that has been usually enforced outright in this study during modelling of multikinetic samples in the past using AFTINV and is apparent upon inspecting sample 07CYA-M38B models. The kinetic population most similar to

typical fluorapatite composition (best characterized examples provided by annealing experiments of Carlson et al. [34]) is held kinetically fixed during thermal-history modelling, whereas end-member populations ordinarily require adjustment to either higher or lower kinetic values outside of the calculated range. This is often necessary because the aforementioned annealing experiments did not fully capture all apatite compositions (or exotic compositions) that are either high or low retentivity with respect to common fluorapatite. The need for kinetic-parameter adjustment is also apparent in the revised annealing-model data fits that were a result of the Ketcham et al. [70] annealing model, when a data set of (mainly) apatite with a high concentration of Cl was added to the Ketcham et al. [68] data set and extrapolated to geological time scales. The sample 07CYA-M38B kinetic populations show that kinetic population no. 2, which has a common fluorapatite composition, based on an eCl value of 0.0 apfu (r_{mr0} = 0.840; see model in Ketcham et al. [68]), is predicted to be the same as the observed mean kinetic-parameter value (i.e., requires no adjustment). However, in both model scenarios the first (low retentivity) and third (high retentivity) populations are driven to lower and higher retentivity with respect to their measured ranges.

Appendix

8.1 Analytical Procedures

Apatite grains were prepared by GeoSep Services, located in Moscow, Idaho, for laser-ablation inductively coupled plasma mass spectrometer (LA-ICP-MS), apatite fission-track (AFT), and accompanying apatite U-Pb analyses using analytical methods presented in Donelick et al. [19] and Chew and Donelick [41]. The Mendeley Data repository [96] also has relevant information on LA-ICP-MS analytical methods and age calculations. Each sample for AFT analysis underwent standard mineral separation (i.e., crushing, heavy liquids density separation, panning) designed to maximize apatite yields. Subsequently, at least one epoxy grain mount (approximately 1 cm^2) was made for each sample, consisting of apatite grains for age and length measurements carried out by analyst P. O'Sullivan of GeoSep Services. Each grain mount was cured at 60 °C for at least four hours, after which each mount was manually polished to a glass-like finish using 3.0 μm and 0.3 μm Al_2O_3 slurries to first expose, and then polish internal grain surfaces. The grain mounts were then immersed in 5.5 M HNO_3 for 20.0 seconds (± 0.5 s) at 21 °C (± 1 °C) to etch and reveal natural fission tracks that intersected the polished grain surfaces. During analyses, etch pit diameter (D_{par}), spontaneous (N_s) track counts, and confined track-length measurements were carried out using unpolarized light at 2000x magnification (100x dry objective, 1.25x projection tube, 16x oculars) and, when possible, each AFT analysis included up to 40 single-grain ages and up to 150 confined track-length measurements. Apatite grains were analyzed for 13 elements (F, Na, Mg, P, S, Cl, Ca, Mn, Fe, Sr, Y, La, and Ce) by electron probe microanalysis at the Peter Hooper Geoanalytical Laboratory of Washington State University using a JEOL JXA8500F Field Emission Electron Microprobe operated at 15 kV (20nA current) with a beam size of 5 μm. All LA-ICP-MS AFT analyses were carried out at Washington State University in Pullman, Washington, using the conditions and parameters outlined below.

LA-ICP-MS operating conditions and data-acquisition parameters

ICP-MS: operating conditions

- Instrument Finnegan Element II Magnetic Sector ICP-MS
- Forward power 1.25 kW
- Reflected power <5 W
- Plasma gas Ar
- Coolant flow 15 L/min
- Carrier flow 1.0 L/min (Ar) 0.8 L//min (He) – daily optimization
- Auxiliary flow 0.9 L/min

ICP-MS: acquisition parameters

- Dwell time 18 ms/peak point
- Points per peak 4
- Mass window 5%
- Scans 30
- Data acquisition time 22 s
- Acquisition mode electron scanning
- Isotopes measured ^{43}Ca, ^{238}U, ^{232}Th, and ^{147}Sm

Laser: operating conditions

- Laser type New Wave UP213 (Nd:YAG)
- Wavelength 213 nm
- Laser mode Q switched
- Laser output power 8 J/cm
- Laser warm-up time 6 s
- Shot repetition rate 5 Hz
- Sampling scheme single spot (16 μm AFT)

For each age grain analyzed, the location on the mount was digitally recorded, D_{par} was measured, and the natural fission-track densities were counted. These grain locations were then revisited using the LA-ICP-MS, where a single spot analysis (16 μm) determined the concentration of U and Th on the same areas of each grain from which the natural fission-track densities were first counted. Then, LA-ICP-MS was used to determine the ^{238}U concentrations by measuring the ratio of ^{238}U to ^{43}Ca from the area on the individual grains from which the spontaneous tracks were counted [40, 19]. The fundamental assumption is that Ca occurs in stoichiometric amounts in all apatite grains analyzed by LA-ICP-MS. The isotope ^{43}Ca is used as the indicator of the volume of apatite ablated and carried out in a helium atmosphere to reduce condensation and elemental fractionation. Fixed-point laser spot analyses were performed and a total of 55 scans for ^{238}U, ^{232}Th, ^{147}Sm, and ^{43}Ca were recorded for each spot analyzed. Of these scans, approximately 10 were performed while the laser was warming up and was blocked from contacting the grain surface; during this time, background counts were collected. Once the laser was permitted to hit the grain surface, a cylindrical pit was excavated to a depth of approximately 16 μm, well beyond the depth (~8 μm) at which U contributes fission tracks to the etched grain surface. Between 30 and 40 scans performed during pit excavation were required to reach this depth. The depths of a representative number of these pits were measured and the ^{238}U/^{43}Ca value was determined based on the weighted mean of the ^{238}U/^{43}Ca value for individual scans relative to the depths from which the ablated material was derived. Uranium values are down-pit weighted to approximately 8 μm depth (or half the length of a fresh track), beyond which tracks do not contribute to the count surface. The fission-track ages and errors were calculated, using: a) the ratio of the density of natural fission tracks present in the grain to the amount of ^{238}U present, and b) a modified version of the radioactive-decay equation that includes a LA-ICP-MS ζ-calibration factor (see equations 1b for age equation and 2b for error calculation in Donelick et al. [19]). This ζ-calibration factor is determined for each sample analyzed during each LA-ICP-MS session by analyzing the U:Ca ratio of an apatite calibration standard of known age (Durango apatite, 30.6 ± 0.3 Ma) at the beginning and end of each LA-ICP-MS session.

ACKNOWLEDGEMENTS

The authors thank Geological Survey of Canada colleagues Denis Lavoie and Lisel Currie for thorough reviews of this paper. They thank Paul O'Sullivan of GeoSep Services for his expert AFT dating efforts. They also thank Michel Plouffe, Paul Wozniak, and Marlene Francis, also from the Geological Survey of Canada, for coordination and support during the GEM-2 program. They would also like to acknowledge all the people and organizations that provided samples, including Michelle Nicolas (Manitoba Geological Survey); Derek Amstrong (Ontario Geological Survey); and Bill Davis and Nicole Rayner (Geological Survey of Canada) for facilitating access to the geochronology sample archive in Ottawa. Thanks also to other Geological Survey of Canada colleagues Natasha Wodicka, Rob Berman, John Percival, Rob Rainbird, Charlie Jefferson, Tony Peterson, Sally Pehrsson, and Jeremy Powell for their assistance in chasing down rocks and for discussions related to this research.

References

[1] Paul F Hoffman. United plates of America, the birth of a craton: Early Proterozoic assembly and growth of Laurentia. *Annual Review of Earth and Planetary Sciences*, 16(1):543–603, 1988.

[2] Paul F Hoffman. Precambrian geology and tectonic history of North America. In A W Bally and A R Palmer, editors, *The geology of North America—an overview*, volume A, chapter 16, pages 447–512. The Geological Society of America, 1989.

[3] Steven J Whitmeyer and Karl E Karlstrom. Tectonic model for the Proterozoic growth of North America. *Geosphere*, 3(4):220–259, 2007.

[4] J W Ambrose. Exhumed paleoplains of the Precambrian Shield of North America. *American Journal of Science*, 262:817–857, 1964.

[5] R M Flowers, S A Bowring, and P W Reiners. Low long-term erosion rates and extreme continental stability documented by ancient (U-Th)/He dates. *Geology*, 34 (11):925–928, 2006. doi: 10.1130/g22670a.1.

[6] T J Blackburn, S A Bowring, J T Perron, K H Mahan, F O Dudas, and K R Barnhart. An Exhumation History of Continents over Billion-Year Time Scales. *Science*, 335(6064):73–76, 2012.

[7] Rebecca M. Flowers, Alexis K. Ault, Shari A. Kelley, Nan Zhang, and Shijie Zhong. Epeirogeny or eustasy? Paleozoic-Mesozoic vertical motion of the North American continental interior from thermochronometry and implications for mantle dynamics. *Earth and Planetary Science Letters*, 317-318(0):436–445, 2012. ISSN 0012821X. doi: 10.1016/j.epsl.2011.11.015.

[8] Kalin T. McDannell, Peter K. Zeitler, and David A. Schneider. Instability of the southern Canadian Shield during the late Proterozoic. *Earth and Planetary Science Letters*, 490:100–109, 2018. ISSN 0012821X. doi: 10.1016/j.epsl.2018.03.012.

[9] Peter M. Burgess. Phanerozoic Evolution of the Sedimentary Cover of the North American Craton. In *The Sedimentary Basins of the United States and Canada*, volume 5, pages 39–75. Elsevier, 2019. ISBN 9780444638953. doi: 10.1016/B978-0-444-63895-3.00002-4.

[10] Carolina Lithgow-Bertelloni and Paul G Silver. Dynamic topography, plate driving forces and the African superswell. *Nature*, 395(6699):269–272, 1998.

[11] RiXiang Zhu, YiGang Xu, Guang Zhu, HongFu Zhang, QunKe Xia, and TianYu Zheng. Destruction of the North China craton. *Science China Earth Sciences*, 55(10): 1565–1587, 2012.

[12] Jean Braun, François Guillocheau, Cécile Robin, Guillaume Baby, and Hielke Jelsma. Rapid erosion of the Southern African Plateau as it climbs over a mantle superswell. *Journal of Geophysical Research: Solid Earth*, 119(7):6093–6112, 2014.

[13] P F Green and I R Duddy. Interpretation of apatite (U–Th)/He ages and fission track ages from cratons. *Earth and Planetary Science Letters*, 244(3-4):541–547, 2006.

[14] Rebecca M Flowers. Exploiting radiation damage control on apatite (U–Th)/He dates in cratonic regions. *Earth and Planetary Science Letters*, 277(1-2):148–155, 2009. doi: 10.1016/j.epsl.2008.10.005.

[15] Kalin T. McDannell. *Methods and application of deep-time thermochronology: Insights from slowly cooled terranes of Mongolia and the North American craton*. PhD thesis, Lehigh University, Bethlehem, Pennsylvania, 2017. URL https://preserve.lehigh.edu/etd/2721.

[16] Kalin T. McDannell, David A. Schneider, Peter K. Zeitler, Paul B. O'Sullivan, and Dale R. Issler. Reconstructing deep-time histories from integrated thermochronology: An example from southern Baffin Island, Canada. *Terra Nova*, 31(3):189–204, 3 2019. doi: 10.1111/ter.12386.

[17] Barry Kohn and A Gleadow. Application of Low-Temperature Thermochronology to Craton Evolution. In Marco G Malusá and Paul G Fitzgerald, editors, *Fission-Track Thermochronology and its Application to Geology*, chapter 21, pages 373–393. Springer, Cham., 2019.

[18] Kalin T. McDannell and Rebecca M. Flowers. Vestiges of the Ancient: Deep-Time Noble Gas Thermochronology. *Elements*, 16(5):325–330, 2020. doi: 10.2138/gselements.16.5.325.

[19] Raymond A Donelick, Paul B O'Sullivan, and Richard A Ketcham. Apatite fission-track analysis. In *Reviews in Mineralogy and Geochemistry*, volume 58, pages 49–94. 2005. ISBN 1529-6466.

[20] Takahiro Tagami and Paul B. O'Sullivan. Fundamentals of fission-track thermochronology. In Peter W. Reiners and Todd A. Ehlers, editors, *Reviews in Mineralogy and Geochemistry*, volume 58, chapter 2, pages 19–47. Mineralogical Society of America and Geochemical Society, Washington, DC, United States (USA), 2005. doi: 10.2138/rmg.2005.58.2.

[21] P B Price and R M Walker. Fossil tracks of charged particles in mica and the age of minerals. *Journal of Geophysical Research*, 68(16):4847–4862, 1963.

[22] R L Fleischer, P B Price, and R M Walker. Tracks of charged particles in solids. *Science*, 149:383–393, 1965.

[23] G A Wagner. Fission track dating of apatites. *Earth and Planetary Science Letters*, 4(5):411–415, 1968.

[24] C W Naeser and Henry Faul. Fission track annealing in apatite and sphene. *Journal of Geophysical Research*, 74 (2):705–710, 1969.

[25] A. J.W. Gleadow and I. R. Duddy. A natural long-term track annealing experiment for apatite. *Nuclear Tracks*, 5(1-2):169–174, 1981. ISSN 0191278X. doi: 10.1016/0191-278X(81)90039-1.

[26] A J W Gleadow, I R Duddy, P Fo Green, and J F Lovering. Confined fission track lengths in apatite: a diagnostic tool for thermal history analysis. *Contributions to Mineralogy and Petrology*, 94(4):405–415, 1986.

[27] Andrew J W Gleadow, Ian R Duddy, Paul F Green, and Kerry A Hegarty. Fission track lengths in the apatite annealing zone and the interpretation of mixed ages. *Earth and Planetary Science Letters*, 78(2-3):245–254, 1986.

[28] P F Green, I R Duddy, A J W Gleadow, P R Tingate, and G M Laslett. Fission-track annealing in apatite: track length measurements and the form of the Arrhenius plot. *Nuclear Tracks and Radiation Measurements*, 10(3):323–328, 1985.

[29] I R Duddy, P F Green, and G M Laslett. Thermal annealing of fission tracks in apatite 3. Variable temperature behaviour. *Chemical Geology: Isotope Geoscience section*, 73(1):25–38, 1988.

[30] P F Green. The relationship between track shortening and fission track age reduction in apatite: combined influences of inherent instability, annealing anisotropy, length bias and system calibration. *Earth and Planetary Science Letters*, 89(3-4):335–352, 1988.

[31] W. D. Carlson. Mechanisms and kinetics of apatite fission-track annealing. *American Mineralogist*, 75(9-10):1120–1139, 1990. ISSN 0003004X.

[32] Kevin D. Crowley, Maryellen Cameron, and Brian J. McPherson. Annealing of etchable fission-track damage in F-, OH-, Cl- and Sr-apatite. 1. Systematics and preliminary interpretations. *Nuclear Tracks and Radiation Measurements*, 17(3):409–410, 1990. ISSN 0191278X. doi: 10.1016/1359-0189(90)90066-7.

[33] C E Ravenhurst, M K Roden, S D Willett, and D S Miller. Dependence of fission track annealing kinetics on apatite crystal chemistry. *Nuclear Tracks and Radiation Measurements*, 21(4):622, 1993.

[34] William D. Carlson, Raymond A. Donelick, and Richard A. Ketcham. Variability of apatite fission-track annealing kinetics: I. Experimental results. *American Mineralogist*, 84(9):1213–1223, 1999. ISSN 0003004X. doi: 10.2138/am-1999-0901.

[35] Jocelyn Barbarand, Andrew Carter, Ian Wood, and Tony Hurford. Compositional and structural control of fission-track annealing in apatite. *Chemical Geology*, 198(1-2):107–137, 2003. ISSN 00092541. doi: 10.1016/S0009-2541(02)00424-2.

[36] Casey E. Ravenhurst, Mary K. Roden-Tice, and Donald S. Miller. Thermal annealing of fission tracks in fluorapatite, chlorapatite, manganoanapatite, and Durango apatite: Experimental results. *Canadian Journal of Earth Sciences*, 40(7):995–1007, 2003. ISSN 00084077. doi: 10.1139/e03-032.

[37] Carlos A. Tello, Rosane Palissari, Julio C. Hadler, Pedro J. Iunes, Sandro Guedes, Eduardo A.C. Curvo, and Sergio R. Paulo. Annealing experiments on induced fission tracks in apatite: Measurements of horizontal-confined track lengths and track densities in basal sections and randomly oriented grains. *American Mineralogist*, 91(2-3):252–260, 2006. ISSN 0003004X. doi: 10.2138/am.2006.1269.

[38] Marco G. Malusà and Paul G. Fitzgerald. *Fission-Track Thermochronology and its Application to Geology*. Springer, Cham., 1 edition, 2019. ISBN 978-3-319-89421-8. doi: 10.1007/978-3-319-89421-8.

[39] Andrew J W Gleadow, David X Belton, Barry P Kohn, and Roderick W Brown. Fission track dating of phosphate minerals and the thermochronology of apatite. *Reviews in Mineralogy and Geochemistry*, 48(1):579–630, 2002.

[40] Noriko Hasebe, Jocelyn Barbarand, Kym Jarvis, Andrew Carter, and Anthony J. Hurford. Apatite fission-track chronometry using laser ablation ICP-MS. *Chemical Geology*, 207(3-4):135–145, 2004. ISSN 00092541. doi: 10.1016/j.chemgeo.2004.01.007.

[41] David M Chew and Raymond A Donelick. Combined apatite fission track and U-Pb dating by LA-ICP-MS and its application in apatite provenance analysis. *Quantitative mineralogy and microanalysis of sediments and sedimentary rocks: Mineralogical Association of Canada Short Course*, 42:219–247, 2012.

[42] Nathan Cogné, David M. Chew, Raymond A. Donelick, and Claire Ansberque. LA-ICP-MS apatite fission track dating: A practical zeta-based approach. *Chemical Geology*, 531, 2020. ISSN 00092541. doi: 10.1016/j.chemgeo.2019.119302.

[43] D R Issler, A M Grist, and L D Stasiuk. Post-Early Devonian thermal constraints on hydrocarbon source rock maturation in the Keele Tectonic Zone, Tulita area, NWT, Canada, from multi-kinetic apatite fission track thermochronology, vitrinite reflectance and shale compaction. *Bulletin of Canadian Petroleum Geology*, 53(4):405–431, 2005.

[44] D R Issler, L S Lane, and P B O'Sullivan. Characterisation, interpretation and modelling of multi-kinetic apatite fission track data using elemental data. Technical report, Geological Survey of Canada, Scientific Presentation 94, https://doi.org/10.4095/311302, 2018. URL https://doi.org/10.4095/311302.

[45] D A Schneider and D R Issler. Application of low-temperature thermochronology to hydrocarbon exploration. In Marco Giovanni Malusa and Paul Fitzgerald, editors, *Fission-Track Thermochronology and its Application to Geology*, chapter 18, pages 315–333. Springer International Publishing, New York, 1 edition, 2019. ISBN 978-3-319-89419-5. doi: 10.1007/978-3-319-89421-8.

[46] Richard A. Ketcham. Technical Note: Calculation of stoichiometry from EMP data for apatite and other phases

with mixing on monovalent anion sites. *American Mineralogist*, 100(7):1620–1623, 2015. ISSN 19453027. doi: 10.2138/am-2015-5171.

[47] Jeremy W. Powell, David A. Schneider, and Dale R. Issler. Application of multi-kinetic apatite fission track and (U-Th)/He thermochronology to source rock thermal history: a case study from the Mackenzie Plain, NWT, Canada. *Basin Research*, 30:497–512, 2018. ISSN 13652117. doi: 10.1111/bre.12233.

[48] Kalin T McDannell and Dale R Issler. Simulating sedimentary burial cycles – Part 1: Investigating the role of apatite fission track annealing kinetics using synthetic data. *Geochronology Discussions*, 2021. doi: 10.5194/gchron-2020-35. URL https://gchron.copernicus.org/preprints/gchron-2020-35/.

[49] Rex F Galbraith. The radial plot: graphical assessment of spread in ages. *International Journal of Radiation Applications and Instrumentation. Part D. Nuclear Tracks and Radiation Measurements*, 17(3):207–214, 1990.

[50] R F Galbraith and P F Green. Estimating the component ages in a finite mixture. *International Journal of Radiation Applications and Instrumentation. Part D. Nuclear Tracks and Radiation Measurements*, 17(3):197–206, 1990.

[51] R F Galbraith and G M Laslett. Statistical models for mixed fission track ages. *Nuclear Tracks and Radiation Measurements*, 21:459–470, 1993.

[52] Gale C. Blackmer, Gomaa I. Omar, and David P. Gold. Post-Alleghanian unroofing history of the Appalachian Basin, Pennsylvania, from apatite fission track analysis and thermal models. *Tectonics*, 13(5):1259–1276, 1994. ISSN 19449194. doi: 10.1029/94TC01507.

[53] Paul O'Sullivan. Statistical evaluation (and manipulation) of fission-track single-grain age data: an analyst's "unbiased" perspective. In *16th International Conference on Thermochronology*, Palais Salfeldt, Quedlinburg, Germany, 2018. Thermo2018. URL https://www.thermo2018.de/content/download/thermo2018_abstracts.pdf.

[54] B W H Hendriks and T F Redfield. Apatite fission track and (U-Th)/He data from Fennoscandia: An example of underestimation of fission track annealing in apatite. *Earth and Planetary Science Letters*, 236(1-2):443–458, 2005.

[55] K T McDannell, D R Issler, and P B O'Sullivan. Radiation-enhanced fission track annealing revisited and consequences for apatite thermochronometry. *Geochimica et Cosmochimica Acta*, 252:213–239, 2019. doi: https://doi.org/10.1016/j.gca.2019.03.006.

[56] Barry P Kohn, Matevz Lorencak, Andrew J W Gleadow, Fabian Kohlmann, Asaf Raza, Kirk G Osadetz, and Peter Sorjonen-Ward. A reappraisal of low-temperature thermochronology of the eastern Fennoscandia Shield and radiation-enhanced apatite fission-track annealing. *Geological Society, London, Special Publications*, 324(1):193–216, 2009.

[57] S Ouchani, J-C Dran, and J Chaumont. Evidence of ionization annealing upon helium-ion irradiation of predamaged fluorapatite. *Nuclear Instruments and Methods in Physics Research Section B: Beam Interactions with Materials and Atoms*, 132(3):447–451, 1997.

[58] Weixing Li, Yahui Shen, Yueqing Zhou, Shuai Nan, Chien-Hung Chen, and Rodney C Ewing. In situ TEM observation of alpha-particle induced annealing of radiation damage in Durango apatite. *Scientific reports*, 7(1):14108, 2017.

[59] Weixing Li, Yuanyuan Cheng, Lei Feng, Jingjing Niu, Yingxin Liu, Vladimir A. Skuratov, Maxim V. Zdorovets, Lynn A. Boatner, and Rodney C. Ewing. Alpha-decay induced shortening of fission tracks simulated by in situ ion irradiation. *Geochimica et Cosmochimica Acta*, 299:1–14, 2021. ISSN 00167037. doi: 10.1016/j.gca.2021.01.022.

[60] Joëlle Carpéna, Jean-Robert Kienast, Khadidja Ouzegane, and Célestine Jehanno. Evidence of the contrasted fission-track clock behavior of the apatites from In Ouzzal carbonatites (northwest Hoggar): The low-temperature thermal history of an Archean basement. *Geological Society of America Bulletin*, 100:1237–1243, 1988.

[61] J Carpéna. Uranium-235 Fission Track Annealing in Minerals of the Apatite Group: An Experimental Study. In P van den Haute and F de Corte, editors, *Advances in Fission-Track Geochronology*, volume 10. Solid Earth Sciences Library, Springer Dordrecht, 1998. doi: 10.1007/978-94-015-9133-1{_}6.

[62] Joëlle Carpéna and Jean-Louis Lacout. Thermal annealing of fission tracks in synthetic apatites. *Nuclear Instruments and Methods in Physics Research Section B: Beam Interactions with Materials and Atoms*, 268(19):3191–3194, 2010.

[63] Pieter Vermeesch. RadialPlotter: a Java application for for fission track, luminescence, and other radial plots. *Radiation Measurements*, 44:409–410, 2009.

[64] Pieter Vermeesch. On the visualisation of detrital age distributions. *Chemical Geology*, 312:190–194, 2012.

[65] Pieter Vermeesch. Statistics for Fission-Track Thermochronology. In Marco Giovanni Malusa and Paul Fitzgerald, editors, *Fission-Track Thermochronology and its Application to Geology*, chapter 6, pages 109–122. Springer International Publishing, New York, 1 edition, 2019.

[66] Kalin T. McDannell. Notes on statistical age dispersion in fission-track datasets: the chi-square test, annealing variability, and analytical considerations. *EarthArXiv*, pages 1–4, 2020. doi: 10.31223/OSF.IO/UJ4HX. URL https://doi.org/10.31223/osf.io/uj4hx.

[67] Pieter Vermeesch and Yuntao Tian. Thermal history modelling: HeFTy vs. QTQt. *Earth-Science Reviews*, 139:279–290, 2014.

[68] Richard A. Ketcham, Raymond A. Donelick, and William D. Carlson. Variability of apatite fission-track annealing kinetics: III. Extrapolation to geological time scales. *American Mineralogist*, 84(9):1235–1255, 1999. ISSN 0003004X. doi: 10.2138/am-1999-0903.

[69] Dale R. Issler, Kalin T. McDannell, Paul B. O'Sullivan, and Larry S. Lane. Simulating sedimentary burial cycles – Part 2: Elemental-based multikinetic apatite fission-track interpretation and modelling techniques illustrated using examples from northern Yukon. (in preparation), 2021.

[70] Richard A. Ketcham, Andrew Carter, Raymond A. Donelick, Jocelyn Barbarand, and Anthony J. Hurford. Improved modeling of fission-track annealing in apatite. *American Mineralogist*, 92(5-6):799–810, 2007. ISSN 0003004X. doi: 10.2138/am.2007.2281.

[71] Dale R Issler. An inverse model for extracting thermal histories from apatite fission track data: instructions and software for the Windows 95 environment. Technical report, Geological Survey of Canada, Open File Report 2325, 1996. URL https://doi.org/10.4095/208313.

[72] Richard A. Ketcham. Forward and inverse modeling of low-temperature thermochronometry data. In *Reviews in Mineralogy and Geochemistry*, volume 58, pages 275–314. 2005. doi: 10.2138/rmg.2005.58.11.

[73] Kerry Gallagher. Transdimensional inverse thermal history modeling for quantitative thermochronology. *Journal of Geophysical Research: Solid Earth*, 117(B2), 2012.

[74] Sean D. Willett. Inverse modeling of annealing of fission tracks in apatite 1: A controlled random search method. *American Journal of Science*, 297(10):939–969, 1997. ISSN 00029599. doi: 10.2475/ajs.297.10.939.

[75] Wyn L Price. A controlled random search procedure for global optimisation. *The Computer Journal*, 20(4): 367–370, 1977.

[76] T Mark Harrison, Marty Grove, Oscar M Lovera, and Peter K Zeitler. Continuous Thermal Histories from Inversion of Closure Profiles. *Reviews in Mineralogy and Geochemistry*, 58(1):389–409, 2005. doi: 10.2138/rmg.2005.58.15.

[77] Jeremy W. Powell, Dale R. Issler, David A. Schneider, Karen M. Fallas, and Daniel F. Stockli. Thermal history of the Mackenzie Plain, Northwest Territories, Canada: Insights from low-temperature thermochronology of the Devonian Imperial Formation. *Bulletin of the Geological Society of America*, 132(3-4):767–783, 2020. ISSN 19432674. doi: 10.1130/B35089.1.

[78] Nicolas Pinet and Virginia Brake. Preliminary compilation of apatite fission-track data in Canada. Technical report, Geological Survey of Canada, Open File 8454, 2018. URL https://doi.org/10.4095/308443.

[79] D R Issler, C Beaumont, S D Willett, R A Donelick, J Mooers, and A Grist. Preliminary evidence from apatite fission-track data concerning the thermal history of the Peace River Arch region, Western Canada Sedimentary Basin. *Bulletin of Canadian Petroleum Geology*, 38(1): 250–269, 1990.

[80] Charles W Naeser and Kevin D Crowley. Fission-track dating of apatite from deep borehole ATK-1 at Atikokan, Ontario. *International Atomic Energy Agency*, 1990.

[81] K. D. Crowley. Thermal history of Michigan Basin and southern Canadian Shield from apatite fission track analysis. *Journal of Geophysical Research*, 96(B1):697–711, 1991. ISSN 01480227. doi: 10.1029/90JB02174.

[82] Casey E Ravenhurst, Sean D Willett, Raymond A Donelick, and Christopher Beaumont. Apatite fission track thermochronometry from central Alberta: Implications for the thermal history of the Western Canada sedimentary basin. *Journal of Geophysical Research: Solid Earth*, 99(B10):20023–20041, 1994. doi: 10.1029/94JB01563.

[83] D C Arne, M Zentilli, A M Grist, and M Collins. Constraints on the timing of thrusting during the Eurekan orogeny, Canadian Arctic Archipelago: an integrated approach to thermal history analysis. *Canadian Journal of Earth Sciences*, 35(1):30–38, 1998.

[84] Dale R Issler, Sean D Willett, Christopher Beaumont, Raymond A Donelick, and Alexander M Grist. Paleotemperature history of two transects across the Western Canada Sedimentary Basin: Constraints from apatite fission track analysis. *Bulletin of Canadian Petroleum Geology*, 47(4):475–486, 1999.

[85] K G Osadetz, B P Kohn, S Feinstein, and P B O'Sullivan. Thermal history of Canadian Williston basin from apatite fission-track thermochronology—implications for petroleum systems and geodynamic history. *Tectonophysics*, 349(1-4):221–249, 2002.

[86] Matevz Lorencak. *Low temperature thermochronology of the Canadian and Fennoscandian Shields: Integration of apatite fission track and (U-Th)/He methods*. PhD thesis, University of Melbourne, 2003.

[87] M Lorencak, B P Kohn, K G Osadetz, and A J W Gleadow. Combined apatite fission track and (U–Th)/He thermochronometry in a slowly cooled terrane: results from a 3440-m-deep drill hole in the southern Canadian Shield. *Earth and Planetary Science Letters*, 227(1): 87–104, 2004.

[88] Alexander M Grist and Marcos Zentilli. The thermal history of the Nares Strait, Kane Basin, and Smith Sound region in Canada and Greenland: constraints from apatite fission-track and (U Th Sm)/He dating. *Canadian Journal of Earth Sciences*, 42(9):1547–1569, 2005.

[89] Barry P Kohn, Andrew J W Gleadow, Roderick W Brown, Kerry Gallagher, Matevz Lorencak, and Wayne P Noble. Visualizing thermotectonic and denudation histories using apatite fission track thermochronology. In Peter W Reiners and Todd A Ehlers, editors, *Reviews in Mineralogy and Geochemistry*, volume 58, pages 527–565. 2005. ISBN 1529-6466. doi: 10.2138/rmg.2005.58.20.

[90] D R Issler and A M Grist. Reanalysis and reinterpretation of apatite fission track data from the central MacKenzie Valley, NWT, Northern Canada: Implications for kinetic parameter determination and thermal modelling. In J I Garver and M J Montario, editors, *11th International Conference on Thermochronology*, pages 130–132, Anchorage, Alaska, 2008. Abstracts with programs. URL https://geoscan.nrcan.gc.ca/starweb/geoscan/servlet.starweb?path=geoscan/fulle.web&search1=R=225530.

[91] Shimon Feinstein, Barry Kohn, Kirk Osadetz, Richard Everitt, and Paul O'Sullivan. Variable Phanerozoic thermal history in the Southern Canadian Shield: Evidence

from an apatite fission track profile at the Underground Research Laboratory (URL), Manitoba. *Tectonophysics*, 475(1):190–199, 2009.

[92] E D McGregor, S B Nielsen, R A Stephenson, K D Petersen, and D I M MacDonald. Long-term exhumation of a Palaeoproterozoic orogen and the role of pre-existing heterogeneous thermal crustal properties: a fission-track study of SE Baffin Island. *Journal of the Geological Society*, 170(6):877–891, 2013.

[93] Nicolas Pinet, Barry Kohn, Denis Lavoie, and Natural Resources Canada. The ups and downs of the Canadian Shield: 1- preliminary results of apatite fission track analysis from Hudson Bay region. *Open File Report 8110*, pages 1–59, 2016. doi: https://doi.org/10.4095/299248.

[94] Alexis K Ault, Rebecca M Flowers, and Samuel A Bowring. Phanerozoic surface history of the Slave craton. *Tectonics*, 32(5):1066–1083, 2013. doi: 10.1002/tect.20069.

[95] D Lavoie, N Pinet, J Dietrich, S Zhang, K Hu, E Asselin, Z Chen, R Bertrand, J Galloway, and V Decker. Geological framework, basin evolution, hydrocarbon system data and conceptual hydrocarbon plays for the Hudson Bay and Foxe basins, Canadian Arctic. *Geological Survey of Canada, Open File Report*, 7363:213, 2013.

[96] Kalin T McDannell, Dale R Issler, and Paul B O'Sullivan. LA-ICP-MS apatite fission track, apatite U-Pb, and electron probe micro-analysis data for the Canadian Shield, 2019. URL http://dx.doi.org/10.17632/wwrkpr9gcx.5.

[97] J. O. Wheeler, P.F. Hoffman, K.D. Card, A. Davidson, B. V. Sanford, A.V. Okulitch, and Roest W.R. Geological map of Canada version 1.0, 1997. URL https://doi.org/10.4095/208175.

[98] W W Heywood and B V Sanford. Geology of Southampton, Coats, and Mansel islands, District of Keewatin, NWT. *Geological Survey of Canada Memoir*, 382:1–35, 1976.

[99] Shunxin Zhang. New insights into Ordovician oil shales in Hudson Bay Basin: their number, stratigraphic position, and petroleum potential. *Bulletin of Canadian Petroleum Geology*, 56(4):300–324, 2008.

[100] S Zhang. Upper Ordovician stratigraphy and oil shales on Southampton Island - field trip guidebook. Technical report, Geological Survey of Canada, Open File 6668, 2010.

[101] Nicolas Pinet, Denis Lavoie, Jim Dietrich, Kezhen Hu, and Pierre Keating. Architecture and subsidence history of the intracratonic Hudson Bay Basin, northern Canada. *Earth-Science Reviews*, 125:1–23, 2013.

[102] Nicolas Pinet, Denis Lavoie, and Pierre Keating. Did the Hudson Strait in Arctic Canada record the opening of the Labrador Sea? *Marine and Petroleum Geology*, 48:354–365, 2013.

[103] D Lavoie, N Pinet, S Zhang, J Reyes, C Jiang, O H Ardakani, M M Savard, R S Dhillon, Z Chen, and J R Dietrich. Hudson Bay, Hudson Strait, Moose River, and Foxe basins: synthesis of the research activities under the Geomapping for Energy and Minerals (GEM) programs 2008-2018, 2019.

[104] S Zhang. Geochemistry data from three oil shale intervals in unit 1, Red Head Rapids Formation (Upper Ordovician) on Southampton Island. Technical report, Geological Survey of Canada, Open File 6681, 2011.

[105] Andrea Schito, Sveva Corrado, Luca Aldega, and Domenico Grigo. Overcoming pitfalls of vitrinite reflectance measurements in the assessment of thermal maturity: the case history of the lower Congo basin. *Marine and Petroleum Geology*, 74:59–70, 2016.

[106] J M Galloway, D A Armstrong, and D Lavoie. Palynology of the INCO Winisk #49204 core (54°18'30"N, 87°02'30"W, NTS 43L/6), Ontario, 2012.

[107] A W Norris and B V Sanford. Paleozoic and Mesozoic geology of the Hudson Bay lowlands. pages 169–205, Ottawa, Ontario, 1968. Geological Survey of Canada, Paper no. 68-53. doi: 10.4095/119794.

[108] P G Telford and D G F Long. Mesozoic geology of the Hudson Platform. In *Elsevier oceanography series*, volume 44, pages 43–54. Elsevier, 1986. ISBN 0422-9894.

[109] B V Sanford. Paleozoic geology of the Hudson Platform. *Canadian Society of Petroleum Geology Special Publications: Sedimentary Basins and Basin-Forming Mechanisms*, — Memoir 1:483–505, 1987.

[110] J A Percival, T Skulski, M Sanborn-Barrie, G M Stott, A D Leclair, M T Corkery, and M Boily. Geology and tectonic evolution of the Superior Province, Canada. *Tectonic Styles in Canada: The Lithoprobe Perspective. Geol Assoc Canada Spec Paper*, 49:321–378, 2012.

[111] D K Armstrong, M P B Nicolas, K E Hahn, and D Lavoie. Stratigraphic synthesis of the Hudson Platform in Manitoba, Ontario, and Nunavut: Ordovician-Silurian. Technical report, Geological Survey of Canada, Open File 8378, 2018.

[112] Shunxin Zhang and John F Riva. The stratigraphic position and the age of the Ordovician organic-rich intervals in the northern Hudson Bay, Hudson Strait, and Foxe basins—evidence from graptolites. *Canadian Journal of Earth Sciences*, 55(8):897–904, 2018. doi: 10.1139/cjes-2017-0266.

[113] A W Norris, A C Grant, B V Sanford, and W R Cowan. Hudson Platform - Geology. In D F Stott and J D Aiken, editors, *Sedimentary cover of the craton in Canada*, volume 5, chapter 8, pages 653–700. Geological Survey of Canada, 1993.

[114] L L Sloss. Sequences in the Cratonic Interior of North America. *Geological Society of America Bulletin*, 74(2):93, 1963. doi: 10.1130/0016-7606(1963)74[93:sitcio]2.0.co;2.

[115] B A Tillement, G Peniguel, and J P Guillemin. Marine Pennsylvanian rocks in Hudson Bay. *Bulletin of Canadian Petroleum Geology*, 24(3):418–439, 1976.

[116] B V Sanford and A C Grant. New findings relating to the stratigraphy and structure of the Hudson Platform. *Geological Survey of Canada, Paper*, 90:17–30, 1990.

[117] T. S. White, B. J. Witzke, and G. A. Ludvigson. Evidence for an Albian Hudson arm connection between the Cretaceous Western Interior Seaway of North America and the Labrador Sea. *Bulletin of the Geological Society of America*, 112(9):1342–1355, 2000. doi: 10.1130/0016-7606(2000)112<1342:EFAAHA>2.0.CO;2.

[118] G D Williams and C R Stelck. Speculations on the Cretaceous paleogeography of North America. In W G E Caldwell, editor, *The Cretaceous System in the Western Interior of North America*, volume Special Pa, pages 1–20. Geological Association of Canada, 1975.

[119] E G Kauffman. Geological and biological overview: Western Interior Cretaceous Basin. *The Mountain Geologist*, 14(3-4):75–99, 1977.

[120] Gerard Bond. Speculations on real sea-level changes and vertical motions of continents at selected times in the Cretaceous and Tertiary Periods. *Geology*, 6(4):247–250, 1978.

[121] Claudia Schröder-Adams. The Cretaceous Polar and Western Interior seas: paleoenvironmental history and paleoceanographic linkages. *Sedimentary Geology*, 301: 26–40, 2014.

[122] J M Kong, D R Boucher, and B H Scott Smith. Exploration and geology of the Attawapiskat kimberlites, James Bay lowland, northern Ontario, Canada. In J J Gurney, J L Gurney, M D Pascoe, and S H Richardson, editors, *7th International Kimberlite Conference*, pages 452–467, Cape Town, South Africa, 1999.

[123] Alexander D McCracken, Derek K Armstrong, and Thomas E Bolton. Conodonts and corals in kimberlite xenoliths confirm a Devonian seaway in central Ontario and Quebec. *Canadian Journal of Earth Sciences*, 37 (12):1651–1663, 2000.

[124] R P Sage. Kimberlites of the Attawapiskat area, James Bay Lowlands, northern Ontario. Technical report, Ontario Geological Survey, Open File Report 6019, 2000. URL http://www.geologyontario.mndm.gov.on.ca/mndmaccess/mndm_dir.asp?type=pub&id=OFR6019.

[125] Kimberley J Webb, Barbara H Scott Smith, Joanne L Paul, and Casey M Hetman. Geology of the Victor Kimberlite, Attawapiskat, Northern Ontario, Canada: cross-cutting and nested craters. *Lithos*, 76(1-4):29–50, 2004.

[126] Nicolas Pinet and Kalin T. McDannell. The ups and downs of the Canadian Shield : 3 – additional apatite fission-track analyses from the Musselwhite, Roberto, Meadowbank and Raglan mines, Ontario, Quebec, and Nunavut. *Geological Survey of Canada, Open File Report 8706*, pages 1–51, 2020. doi: 10.4095/321845.

[127] Rebecca M. Flowers, Richard A. Ketcham, David L. Shuster, and Kenneth A. Farley. Apatite (U-Th)/He thermochronometry using a radiation damage accumulation and annealing model. *Geochimica et Cosmochimica Acta*, 73(8):2347–2365, 2009. ISSN 00167037. doi: 10.1016/j.gca.2009.01.015.

[128] Chloé Gerin, Cécile Gautheron, Erwan Oliviero, Cyril Bachelet, Duval Mbongo Djimbi, Anne-Magali Seydoux-Guillaume, Laurent Tassan-Got, Philippe Sarda, Jérôme Roques, and Frédérico Garrido. Influence of vacancy damage on He diffusion in apatite, investigated at atomic to mineralogical scales. *Geochimica et Cosmochimica Acta*, 197:87–103, 2017.

[129] K Webb, M Harder, P Holmes, M C Baumgartner, and J Pell. The geology of the Nanuq kimberlite: New textural varieties in the Western Churchill Province, Canada. In *9th International Kimberlite Conference: Extended Abstracts*, volume 9, pages 1–3, Frankfurt, Germany, 2008. doi: 10.29173/ikc3534.

[130] S B Nielsen, O R Clausen, and E McGregor. Basin%Ro: a vitrinite reflectance model derived from basin and laboratory data. *Basin Research*, 29:515–536, 2017.

[131] J J Sweeney and Alan K Burnham. Evaluation of a simple model of vitrinite reflectance based on chemical kinetics. *AAPG Bulletin*, 74(10):1559–1570, 1990.

[132] Nicolas Pinet, Kalin T McDannell, Dale R Issler, and Lisel Currie. Characterizing the Phanerozoic history of the Canadian Shield using multi-kinetic apatite fission track analysis – Examples from the Hudson Bay region. In *GAC-MAC-IAH Conference*, Quebec City, Quebec, 2019. URL https://gacmac-quebec2019.ca/wp-content/uploads/2019/05/ABSTRACT-Final-1.pdf.

[133] O M Lovera, Frank M Richter, and T Mark Harrison. The 40Ar/39Ar Thermochronometry for Slowly Cooled Samples Having a Distribution of Diffusion Domain Sizes. *Journal of Geophysical Research*, 94(B12):17917–17935, 1989.

[134] O M Lovera, F M Richter, and T Mark Harrison. Diffusion Domains Determined by 39Ar Released During Step Heating. *Journal of Geophysical Research*, 96(B2): 2057–2069, 1991.

[135] Oscar M Lovera, Marty Grove, and T Mark Harrison. Systematic analysis of K-feldspar 40Ar/39Ar step heating results II: relevance of laboratory argon diffusion properties to nature. *Geochimica et Cosmochimica Acta*, 66(7): 1237–1255, 2002.

[136] Philip A Allen and John J Armitage. Cratonic basins. In Cathy Busby and Antonio Azor, editors, *Tectonics of sedimentary basins: Recent advances*, chapter 30, pages 602–620. Wiley, first edition, 2012. doi: 10.1002/9781444347166.ch30.

[137] J Reyes, C Jiang, D Lavoie, M Milovic, R Robinson, S Zhang, D Armstrong, and A Mort. Determination of hydrocarbon generation and expulsion temperature of organic-rich Upper Ordovician shales from Hudson Bay and Foxe basins using modified hydrous pyrolysis, organic petrography, Rock-Eval and organic solvent extraction. *Geological Survey of Canada, Open File*, 8049: 62, 2016.

[138] S. E. Zurevinski, L. M. Heaman, and R. A. Creaser. The origin of Triassic/Jurassic kimberlite magmatism, Canada: Two mantle sources revealed from the Sr-Nd isotopic composition of groundmass perovskite. *Geochemistry, Geophysics, Geosystems*, 12(9):1–19, 2011. doi: 10.1029/2011GC003659.

[139] Harrison O Cookenboo, Michael J Orchard, and David K Daoud. Remnants of Paleozoic cover on the Archean Canadian Shield: limestone xenoliths from kimberlite in the central Slave craton. *Geology*, 26(5):391–394, 1998.

[140] Lavern D Stasiuk, Art R Sweet, and Dale R Issler. Reconstruction of burial history of eroded Mesozoic strata using kimberlite shale xenoliths, volcaniclastic and crater facies, Northwest Territories, Canada. *International Journal of Coal Geology*, 65(1-2):129–145, 2006.

[141] Shunxin Zhang and Jennifer Pell. Conodonts recovered from the carbonate xenoliths in the kimberlites confirm the Paleozoic cover on the Hall Peninsula, Nunavut. *Canadian Journal of Earth Sciences*, 51(2):142–155, 2014.

[142] P J Patchett, A F Embry, G M Ross, B Beauchamp, J C Harrison, U Mayr, C E Isachsen, E J Rosenberg, and G O Spence. Sedimentary cover of the Canadian Shield through Mesozoic time reflected by Nd isotopic and geochemical results for the Sverdrup Basin, Arctic Canada. *The Journal of Geology*, 112(1):39–57, 2004.

[143] N J MacMillan. Shelves of Labrador Sea and Baffin Bay. *The Future Petroleum Provinces of Canada. Edited by RG McCrossan. Canadian Society of Petroleum Geologists, Memoir*, 1:473–517, 1973.

[144] Alejandra Duk-Rodkin and Owen L Hughes. Tertiary-Quaternary drainage of the pre-glacial Mackenzie Basin. *Quaternary International*, 22:221–241, 1994.

[145] L L Sloss. Tectonic evolution of the craton in Phanerozoic time. *The Geology of North America*, 2:25–51, 1988.

[146] Kerry Gallagher and Richard A. Ketcham. Comment on "Thermal history modelling: HeFTy vs. QTQt" by Vermeesch and Tian, Earth-Science Reviews (2014), 139, 279–290, 2018.